PHYSICAL REVIEW RESEARCH **5**, 033140 (2023)

Impact of disorder in the charge density wave state of Pd-intercalated $\mathrm{ErTe_3}$ revealed by the electrodynamic response

M. Corasaniti,[*] R. Yang,[*,†] and L. Degiorgi[‡]
Laboratorium für Festkörperphysik, ETH–Zürich, 8093 Zürich, Switzerland

J. A. W. Straquadine, A. Kapitulnik, and I. R. Fisher
Geballe Laboratory for Advanced Materials and Department of Applied Physics, Stanford University, Stanford, California 94305, USA
and Stanford Institute for Materials and Energy Sciences, SLAC National Accelerator Laboratory,
2575 Sand Hill Road, Menlo Park, California 94025, USA

(Received 6 April 2023; accepted 25 July 2023; published 29 August 2023)

It is a general notion that disorder, introduced by either chemical substitution or intercalation as well as by electron irradiation, is detrimental to the realization of long-range charge density wave (CDW) order. We study the disorder-induced suppression of in-plane CDW orders in two-dimensional Pd-intercalated $\mathrm{ErTe_3}$ compositions by exploring the real part of the optical conductivity with light polarized along the in-plane a and c axes. Our findings reveal an anisotropic charge dynamics with respect to both incommensurate unidirectional CDW phases of $\mathrm{ErTe_3}$, occurring within the ac plane. The anisotropic optical response gets substantially washed out with Pd intercalation, hand in hand with the suppression of both CDW orders. The spectral weight analysis, though, advances the scenario, for which the CDW phases evolve from a (partially) depleted Fermi surface already above their critical onset temperatures. We therefore argue that the long-range CDW orders of $\mathrm{ErTe_3}$ tend to be progressively dwarfed by Pd intercalation, which favors the presence of short-range CDW segments for both crystallographic directions persisting in a broad temperature (T) interval up to the normal state, and being suggestive of precursor effects of the CDW orders as well as possibly coexisting with superconductivity at low T.

DOI: 10.1103/PhysRevResearch.5.033140

I. INTRODUCTION

The interplay between broken-symmetry ground states, either via competition or coexistence, belongs to the mostly explored topics of modern solid-state physics and seems to be an essential ingredient in the arena of strongly correlated materials. It goes without saying that the discovery of a charge density wave (CDW) phase in the middle of the pseudogap region of the high-temperature superconducting cuprates (HTC) brought into focus the intrinsic nature of those very different cooperative electronic phenomena, suggesting concepts such as intertwined order [1]. However, in HTC and other materials, like the iron-based superconductors, any kind of broken-symmetry ground state also arises in the presence of significant disorder because of the large doping required to destroy the phase of the parent compound (i.e., Mott insulator or magnetic). In the absence of electron-electron interactions, a metal can turn into an Anderson insulator [2] with disorder, but it can remain metallic if interactions are relevant. Therefore, disorder, intended from a broad perspective and induced either by doping or by electron irradiation, cannot be neglected when addressing the emergence of superconductivity from or within a CDW environment.

It is a widespread wisdom of competing orders that the disorder-induced suppression of the CDW state may naturally lead to the increase in the superconducting critical temperature T_c. In a weak coupling picture, CDW suppression increases the number of carriers available for superconductivity pairing at the Fermi surface (FS), thus enhancing T_c. In systems where CDW competes with superconductivity, disorder promoting the latter connotes a very significant physical scenario, which even extends to a strongly coupled situation as long as disorder remains weak. Though there is a need to better scrutinize such a proposition, particularly with model systems capturing the impact of disorder but allowing us to circumvent the complications of strong magnetic correlations or of a Mott insulating phase. In this respect, several old materials were revisited and several new ones were chased. For instance, members of the transition metal dichalcogenide family [3,4] as well as alternative materials like $\mathrm{Cu}_x\mathrm{TiSe_2}$

---

[*] These authors contributed equally to the paper.

[†] Present address: Key Laboratory of Quantum Materials and Devices of Ministry of Education, School of Physics, Southeast University, Nanjing 211189, China.

[‡] Correspondence and requests for materials should be addressed: Laboratorium für Festkörperphysik, ETH–Zürich, 8093 Zürich, Switzerland; degiorgi@solid.phys.ethz.ch

[5–7] were intensively investigated to elucidate how the CDW order gets affected and conversely how superconductivity may be favored by the presence of disorder.

Here, we address the Pd-intercalated ErTe$_3$ (from now on also noted as Pd$_x$ErTe$_3$), which recently arose to a model family of materials serving as suitable playground for a controlled tuning of disorder [8,9], with the intent of tracing its implications from the perspective of the charge dynamics. Our focus is specifically restricted to the optical signatures of the CDW ground state, being the Pd content $x \leqslant 1.2\%$ in our samples (while the onset of superconductivity clearly occurs for $x > 2\%$ [8]). A peculiar asset of the chosen compounds resides in the fact that, unlike the parent ditelluride material where vacancies were found, the (undoped) tritelluride one is free from defects in the Te layers and the accurately tunable Pd intercalation in ErTe$_3$ solely allows a more systematic optical investigation than previous attempts [10,11]. ErTe$_3$ itself originally kindled a lot of attention since it belongs to the wider series of RTe$_3$ (R = Y, La-Nd, Sm, Gd-Tm) quasi-two-dimensional metals exhibiting unidirectional (in-plane) incommensurate CDW states and harbors two successive CDW phase transitions, with critical temperatures $T_{\mathrm{CDW1}} \simeq$ 260 K and $T_{\mathrm{CDW2}} \simeq 160$ K [12–15]. The resistivity [$\rho_{\mathrm{dc}}(T)$] measurements [16] provide signatures for anisotropic transport properties at both CDW phase transitions (i.e., broad bumps overlapped to the otherwise metalliclike $\rho_{\mathrm{dc}}(T)$ for each in-plane a and c axis, Fig. 4 in the Appendix), which are then smeared and suppressed (i.e., lowering of both T_{CDW1} and T_{CDW2}) by the Pd intercalation, consistent with the dominant effect arising from disorder [8].

The absorption spectrum [17] generally gives access to the relevant energy scales [like the CDW gap(s)] and the optical spectral weight (SW) encountered in the charge dynamics as well as its relative temperature (T) evolution shed light on the reconstruction of the electronic band structure and on FS instabilities with respect to the CDW transitions [18–20], here additionally singled out for both the c and a axes [Fig. 4(a) in the Appendix]. We will impart that our present data grasp, first, an anisotropic optical response (missed in previous investigations [21,22]), emerging between the two in-plane crystallographic axes but diminishing with disorder, and, second, emphasize the relevance of CDW precursor effects, the latter present already at $T > T_{\mathrm{CDW1}}$ and evolving into a long-range CDW order at $T < T_{\mathrm{CDW1}}$ and T_{CDW2} in the pristine ($x = 0$) and weakly Pd-intercalated Pd$_x$ErTe$_3$.

II. SAMPLES AND EXPERIMENT

The samples for our optical investigation were grown after a Te self-flux method as described previously for RTe$_3$ (R = rare earth) [23], with the additional small amounts of Pd to the melt. The resulting crystals are orange in color, shiny, soft, and micaceous metals.

The T dependence of the optical reflectivity [$R(\omega)$] at near-normal incidence of light is measured on shiny surfaces, pertaining to the ac plane [Fig. 4(a) in the Appendix] of an approximate size of 1×2 mm^2 for all samples [17]. Measurements were always performed on freshly cleaved (thin) crystals for both polarizations of light along the c and a axes. Data from ~30 to 12 000 cm^{-1}, thus from the far- (FIR), up to the mid- (MIR), and then near-infrared (NIR) spectral ranges, are collected from ~5 to 300 K by using the Fourier transform infrared spectrometer (Bruker Vertex 80v). From NIR up to the ultraviolet (UV) range, i.e., $4\,000 \sim 48\,000\,\mathrm{cm}^{-1}$, $R(\omega)$ is measured at 300 K with the PerkinElmer Lambda 950 spectrometer.

The $R(\omega)$ spectra over the broad FIR-UV spectral range are then an indispensable prerequisite to preform reliable Kramers-Kronig transformation for achieving the real part [$\sigma_1(\omega)$] of the broadband (longitudinal) optical conductivity [17]. We refer to the Appendix for further technical details about the experiment and for a comprehensive review of the original $R(\omega)$ data (Figs. 5–7) and corresponding $\sigma_1(\omega)$ (Figs. 9–11).

III. RESULTS AND DISCUSSION

Introducing our results, we primarily highlight the derived optical anisotropy as a function of T, defined by the $\sigma_1(\omega)$ ratio between the c and a axes [i.e., $\sigma_1^c(\omega, T)/\sigma_1^a(\omega, T)$], shown in Fig. 1 for the FIR up to the MIR spectral range. As pointed out earlier for the pristine compound, this FIR-MIR energy interval mates with the spectral range tied to the characteristic energy scales of the CDW gap(s), located at about 3000 cm^{-1} [21,22,24]. Such an anisotropy in ErTe$_3$ [Fig. 1(a)] is mainly dominated by the peak around 2000 cm^{-1} and the depletion around 5000 cm^{-1}, both coinciding with related absorption features at equivalent energy scales in $\sigma_1(\omega)$ [inset of Fig. 1(a)]. The evolution in T of the intensity in $\sigma_1^c(\omega, T)/\sigma_1^a(\omega, T)$ is quite monotonous upon crossing T_{CDW1} and T_{CDW2}. Moreover, the observed optical anisotropy progressively pales upon increasing the Pd-intercalation content x [Figs. 1(b) and 1(c) and their insets]. Overall, we anticipate that these findings bear testimony to an important reconstruction of the electronic band structure as well as to a substantial spillover effect of the intercalation-driven disorder with respect to both CDW transitions.

Figure 2 underscores anew the anisotropy of the optical response, depicted here by the ratio of the integrated spectral weight $\mathrm{SW}^c(\omega_c, T)/\mathrm{SW}^a(\omega_c, T)$ (Fig. 12 in the Appendix) at selected cutoff frequencies ω_c [26]. We choose two ω_c: at FIR energy scales (i.e., 10–50 cm^{-1}), pertaining to the metallic Drude component of $\sigma_1(\omega)$ [see Figs. 16(b), 16(d), 16(f), 17(b), 17(d), and 17(f) in the Appendix], and at MIR ones (i.e., 600–2400 cm^{-1}), denoting the energy interval with the occurrence of the optical anisotropy affiliated to the interband transitions (Fig. 1). We exert the criterion to set ω_c at MIR frequencies in coincidence with the peak of $\mathrm{SW}^c(\omega_c, T)/\mathrm{SW}^a(\omega_c, T)$ (Fig. 12 in the Appendix). We remark that ω_c is uniquely identified and is virtually constant at $T \leqslant$ 150–200 K, while ω_c turns out to be less precisely defined at higher T. This propagates to the uncertainties in the estimation of the anisotropic $\mathrm{SW}^c(\omega_c, T)/\mathrm{SW}^a(\omega_c, T)$ and is accounted for by the enhanced error bars upon increasing T in Fig. 2.

$\mathrm{SW}^c(\omega_c, T)/\mathrm{SW}^a(\omega_c, T)$ is contrasted with the dc transport anisotropy, represented by the ratio of the dc conductivity along the c and a axes [i.e., $\sigma_{\mathrm{dc}}^c(T)/\sigma_{\mathrm{dc}}^a(T)$] [25]. For ω_c at FIR energy scales, $\mathrm{SW}^c(\omega_c, T)/\mathrm{SW}^a(\omega_c, T)$ mimics the anisotropy of the dc conductivity. On the contrary, for ω_c at

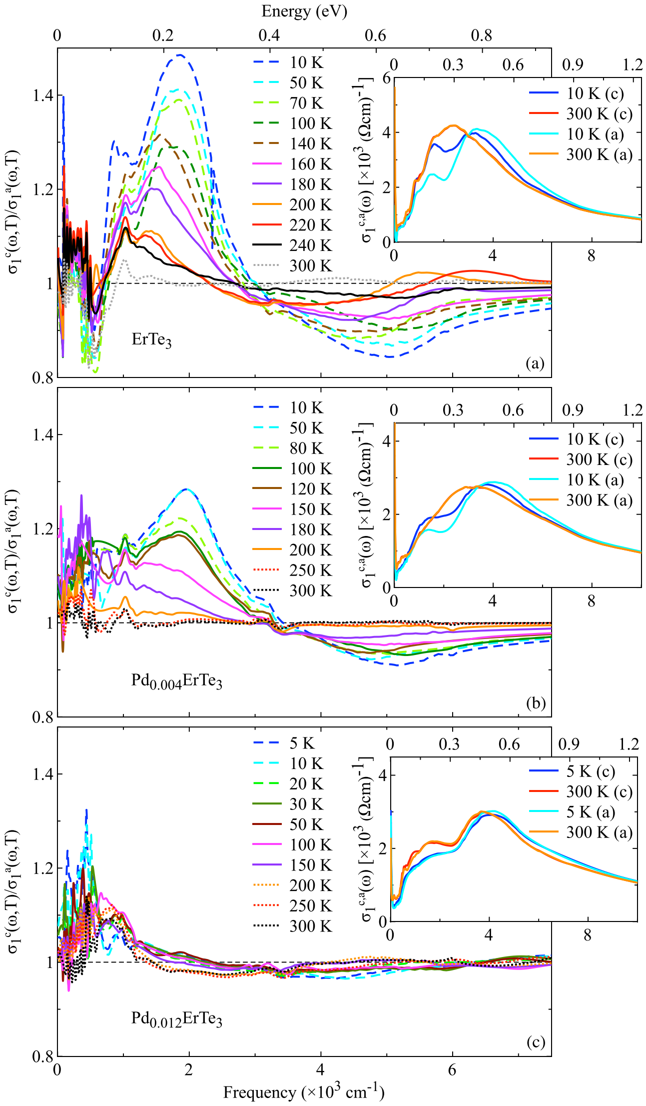

FIG. 1. T dependence of the optical anisotropy, defined by the ratio $\sigma_1^c(\omega,T)/\sigma_1^a(\omega,T)$, for (a) $x = 0$, (b) $x = 0.004$, and (c) $x = 0.012$ Pd$_x$ErTe$_3$ from the FIR up to the MIR energy scales (1 eV = 8.06548×10^3 cm^{-1}). The dotted lines refer to $T > T_{\rm CDW1}$, steady lines to $T_{\rm CDW2} < T < T_{\rm CDW1}$, and dashed lines to $T < T_{\rm CDW2}$. The insets show $\sigma_1(\omega)$ for both the c and a axes at 300 K and 5 or 10 K, as the highest and lowest measured T, respectively, covering the entire spectral range up to the visible frequencies (see the Appendix for further data and details).

MIR energy scales, the optical anisotropy increases gradually, with a change of slope between $T_{\rm CDW1}$ and $T_{\rm CDW2}$ being barely perceptible upon increasing the Pd intercalation. This is already a signature that the conduction bands crossing the Fermi energy (E_F) directly reflect the dc anisotropy as a function of T, while the implications of the CDW states on the electronic band structure at energy scales far away from E_F are somehow more distinct and the resulting (optical) anisotropy is not necessarily copying the dc transportlike behavior across $T_{\rm CDW1}$ and $T_{\rm CDW2}$. It is also worth noting that the anisotropy of all quantities gets considerably reduced upon increasing the Pd-intercalation concentration x.

We stick to the model-independent analysis based on the integrated SW [26] and consider, complementary to Fig. 2, the SW ratio with respect to 300 K, given by SW$^{c,a}(T)$/SW^{c,a}(300 K) and shown as a function of T in Fig. 3 for the a (lower panels) and c (upper panels) axes. The SW ratio at $T < 300$ K clearly emphasizes a twofold SW reallocation to low (with SW ratio above 1) and above all to high (with SW ratio below 1) energies (see also the Appendix for more insights), which gets more pronounced upon decreasing T. This seems to be true for all Pd$_x$ErTe$_3$. Such behavior is anisotropic as well, since the depletion in SW$^{c,a}(T)$/SW^{c,a}(300 K) below 1 is clearly stronger along the a axis than the c axis (at least for $x = 0$ and 0.004); an aspect which may be already recognized directly from the integrated SW (insets of Fig. 3), being at 5 or 10 K in the MIR spectral range decidedly more depleted along the a axis than the c axis with respect to 300 K. The accumulation of SW at low energies for both polarizations occurs in a rather small FIR spectral range, which narrows as well upon decreasing T (for $x = 0$ and 0.004 Pd$_x$ErTe$_3$) or at least at low T (for $x = 0.012$ Pd$_x$ErTe$_3$). This narrowing may be ascribed to the suppression of scattering channels for the itinerant charge carriers in the CDW ground state(s) [Figs. 13(a), 13(c), and 13(e) in the Appendix]. On the other hand, the width at any T of that low-energy SW accumulation becomes visibly larger for the highest Pd intercalation at $x = 0.012$ [Figs. 3(e) and 3(f)], being a direct fingerprint of the enhanced Drude scattering rate along both polarization directions [Fig. 13(e) in the Appendix] as consequence of the Pd-intercalation-induced disorder.

Figure 3 also tells us that a smaller fraction of FS gets gapped by the CDW transitions [18,19] upon increasing the Pd-intercalation concentration x. Indeed, the depletion below 1 of the SW ratio itself is a rough measure of that fraction [29], which is of the order of 10–30% (graphically sketched by the grey areas in Fig. 3). Particularly along the a axis, for which the anomalies in the dc resistivity are remarkably more pronounced than along the c axis [Figs. 4(b)–4(d) in the Appendix], the effective FS gapping tends to shrink with increasing Pd intercalation. We might ponder that the amount of FS gapping along the c axis is less influenced by the Pd intercalation than along the a axis for both (primary and secondary) CDW transitions. The relationship and correspondence between the FS erosion and the anomaly in $\rho_{\rm dc}$ were already advanced in the past [27] in connection with the CDW as well as spin density wave transitions in two-dimensional materials (for which, notoriously, the FS nesting is not as perfect as in one dimension [18–20]). Independent from the origin of the FS gapping or depletion upon which we will return later, we find reasonable agreement within the same bulk values of its estimation from the SW ratio (grey areas in Fig. 3) and the dc transport data (horizontal red-dashed lines in Fig. 3 [28]) of Pd$_x$ErTe$_3$. We caution, however, that the presence of two CDW phase transitions at $T_{\rm CDW1}$ and $T_{\rm CDW2}$ and of the corresponding double anomaly in $\rho_{\rm dc}(T)$ may configure such a comparison as disputable. Nonetheless, this appraisal looks *a posteriori* rather robust. The discrepancy between the two analysis at the $x = 0.012$ Pd intercalation [Figs. 3(e) and 3(f)] is explained by the use of $\rho_{\rm dc}(T)$ for the $x = 0.019$ one [Fig. 4(d) in the Appendix], which consistently dissimulates a smaller FS gapping. As a side note, the frequency

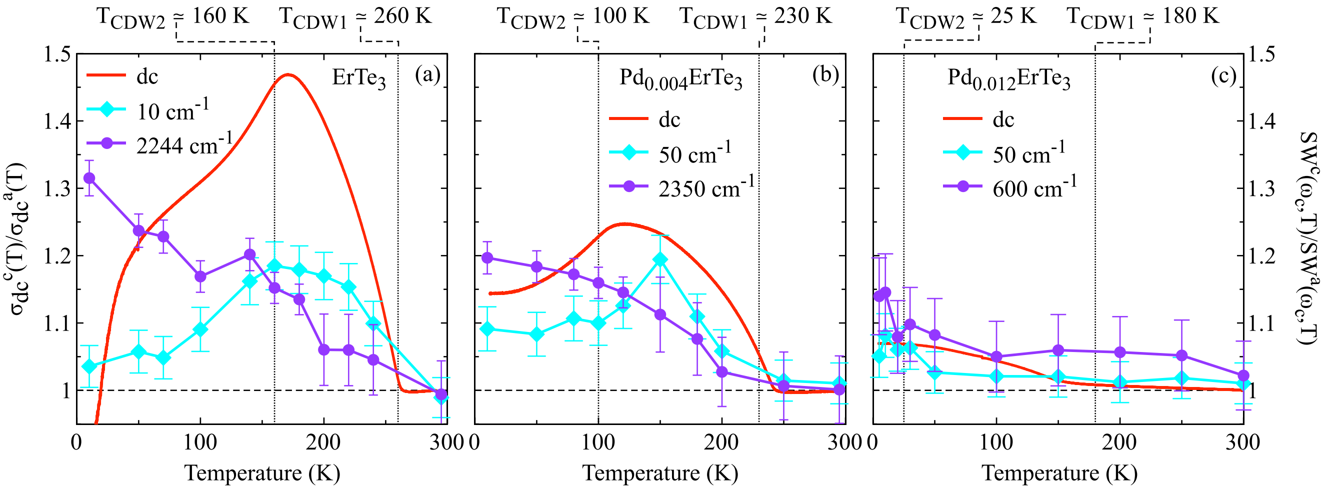

FIG. 2. T dependence of the dc transport anisotropy, defined by $\sigma_{\mathrm{dc}}^{c}(T)/\sigma_{\mathrm{dc}}^{a}(T)$ [with $\sigma_{\mathrm{dc}}(T) = \frac{1}{\rho_{\mathrm{dc}}(T)}$] [25], compared to the anisotropy of the optical SW given by $\mathrm{SW}^{c}(\omega_c, T)/\mathrm{SW}^{a}(\omega_c, T)$ (from Fig. 12 in the Appendix) at selected cutoff frequencies ω_c [26], representing the FIR (i.e., $\omega_c \sim$ 10–50 cm^{-1}, therefore significant for the dc limit of the optical response) and MIR (i.e., $\omega_c \sim$ 600–2400 cm^{-1}) spectral range for (a) $x = 0$, (b) $x = 0.004$, and (c) $x = 0.012$ Pd$_x$ErTe$_3$. The vertical dotted lines mark T_{CDW1} and T_{CDW2} [8]. See text about the origin of the error bars in $\mathrm{SW}^{c}(\omega_c, T)/\mathrm{SW}^{a}(\omega_c, T)$.

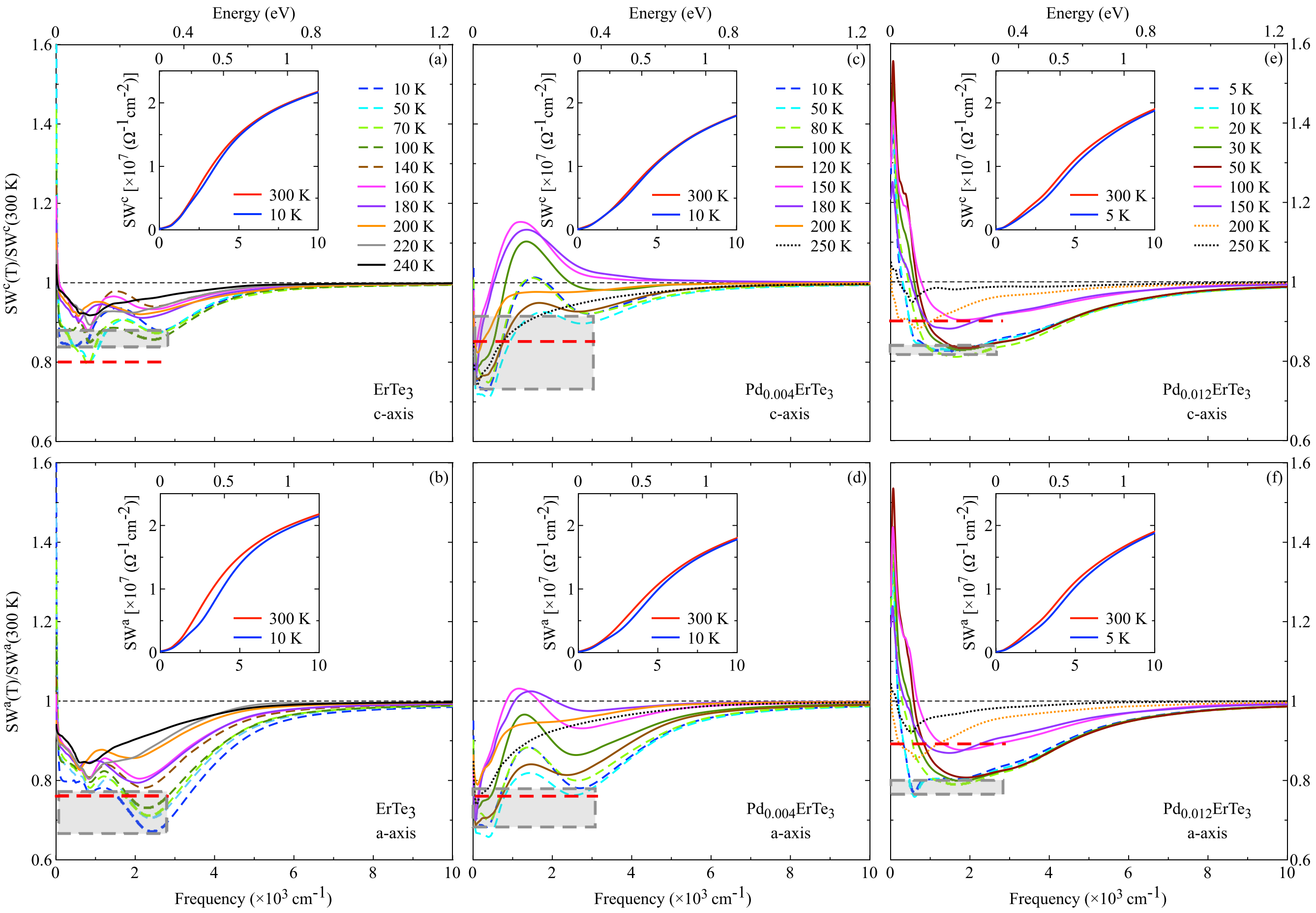

FIG. 3. T dependence of the integrated spectral weight ratio $\mathrm{SW}^{c,a}(T)/\mathrm{SW}^{c,a}(300\,\mathrm{K})$ along the a (lower panels) and c (upper panels) axes for (a), (b) $x = 0$; (c), (d) $x = 0.004$; and (e), (f) $x = 0.012$ Pd$_x$ErTe$_3$. The dotted lines refer to $T > T_{\mathrm{CDW1}}$, steady lines to $T_{\mathrm{CDW2}} < T < T_{\mathrm{CDW1}}$, and dashed lines to $T < T_{\mathrm{CDW2}}$. The range, within which the depletion of the SW ratio occurs at the lowest T across the FIR-MIR energy interval, is noted by the grey areas. It roughly indicates the amount of the FS gapping. The horizontal red-dashed lines represent an estimation [27,28] of the amount of the FS gapping from $\rho_{\mathrm{dc}}(T)$ [8,16,25]. The insets show the integrated $\mathrm{SW}^{c,a}(T)$ at 5 or 10 and 300 K (in units of $\Omega^{-1}\mathrm{cm}^{-2}$ [26]) for each crystallographic axis. Main panels and insets cover the energy spectral range from zero up to $\omega_c \sim 10^4$ cm^{-1} (1 eV = 8.06548×10^3 cm^{-1}), since above this energy scale $\mathrm{SW}^{c,a}(T)$ is fully recovered and conserved at any T [17].

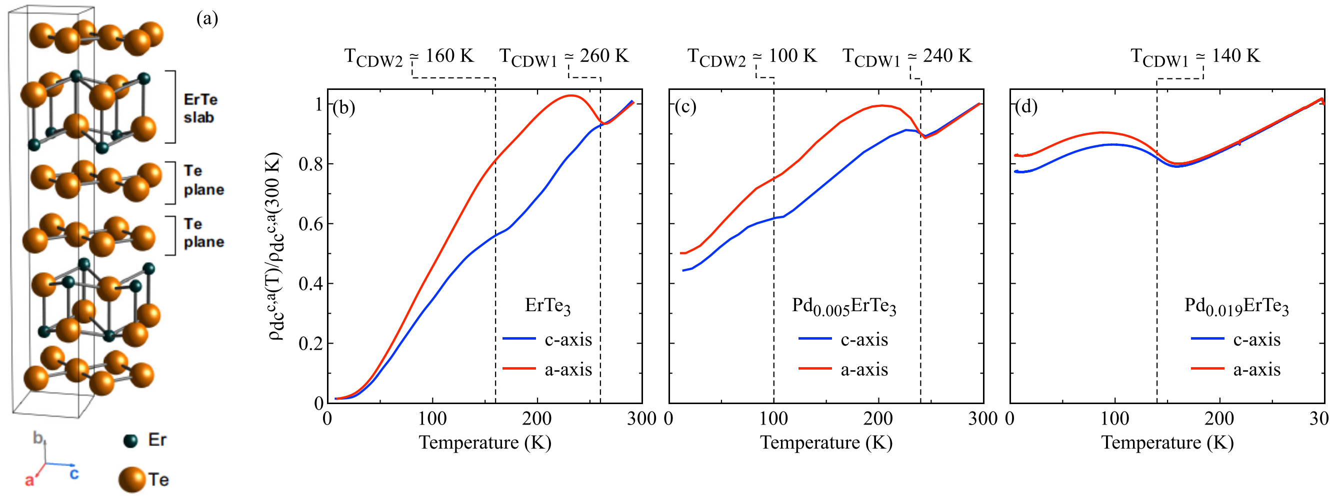

FIG. 4. (a) The original crystal structure of $\mathrm{ErTe_3}$ with the relevant axes is reproduced from Ref. [8]. (b)–(d) T dependence of the dc resistivity $[\rho_{\mathrm{dc}}(T)]$ normalized at 300 K along both the a and c axes for (b) $x = 0$, (c) $x = 0.005$, and (d) $x = 0.019$ $\mathrm{Pd}_x\mathrm{ErTe_3}$, reproduced from Refs. [8,16]. The vertical dashed lines mark T_{CDW1} and T_{CDW2}.

of the deepest minimum in $\mathrm{SW}^{c,a}(T)/\mathrm{SW}^{c,a}(300\,\mathrm{K})$ may be used as an indicative, notwithstanding rough measure of the CDW gap(s) [21,22,24]. We observe a broadening of the minimum in the SW ratio between the $x = 0$ and 0.012 Pd intercalations, testifying an amplified distribution of the gap energy scales and, respectively, an additional manifestation of disorder besides its generated reduction of the effective amount of the FS gapping.

We finally turn our attention to the T dependence of the SW ratio and its consequences towards a possible microscopic model for the interplay between disorder and CDW phase transitions. Foremost, it is worth knowing that a depletion of the SW ratio occurring over an ample T interval, even extending well above the nominal CDW transition temperatures, was also recently observed in $\mathrm{ZrTe}_{3-x}\mathrm{Se}_x$ [30]. In fact, the SW ratio in Fig. 3 is consistently depleted in the MIR spectral range at all T with respect to 300 K along both polarization directions. Admittedly, for $\mathrm{ErTe_3}$ one may argue that the depletion of the SW ratio just happens for T already below T_{CDW1}, since the relatively high T_{CDW1} and our T grid do not allow any firm claim for the optical response of the so-called normal state. However, for the two Pd-intercalated $\mathrm{ErTe_3}$ compositions studied here [Figs. 3(c)–3(f)], it is a well-established experimental fact that the SW removal at MIR frequencies does already happen in the normal state, so at T definitely above the highest CDW transition at T_{CDW1}. Interestingly enough, at $T_{\mathrm{CDW2}} < T < T_{\mathrm{CDW1}}$, an intriguing local recovering of SW is prominently observed in a narrow energy interval around 1000 cm^{-1} for the $x = 0.004$ Pd intercalation [Figs. 3(c) and 3(d)], affecting the low-frequency shoulder of the MIR peak prior to a renewed SW depletion and full recovery at higher energy scales. This latter facet is just adumbrated in the pristine compound [$x = 0$, Figs. 3(a) and 3(b)] and is not at all detected in the spectra of the $x = 0.012$ Pd intercalation [Figs. 3(e) and 3(f)]. While beyond the immediate scope of this paper, we venture a guess that this not-straightforward SW reshuffling in selected spectral ranges underlines the complex evolution of the electronic band structure and its interplay with impurity bands in the intermediate T regime between the two CDW transitions. We refer to the discussion around Figs. 16 and 17 in the Appendix for an alternative analysis of the SW redistribution, pinned down to specific energy intervals.

IV. CONCLUSIONS

The globally emerging picture is tightly bound to the presence of a pseudogap in the electronic excitation spectrum of $\mathrm{Pd}_x\mathrm{ErTe_3}$ in their normal state. Such pseudogaps reveal the tendency towards the formation of short-range order, uncorrelated CDW segments forming already at high T (i.e., in the normal state) and crossing over to a coherent CDW condensate at low T. We conjecture that the Pd intercalation may then perturb the long-range phase coherence of the pristine material by inducing patches of CDW condensates without specific and/or well-defined orientations with respect to the crystallographic structure, as similarly proposed elsewhere [31]. This destroys the bidirectional nature of the CDW transitions, waving the characteristic anisotropy in several physical properties between the crystallographic axes but yet leading to the partial depletion of FS for any Pd intercalation (Fig. 3).

Our optical results therefore convey the relevance of precursors in the formation of the CDW condensate, which certainly are not surprising for genuine CDW materials [19,32,33]. In the latter materials, precursor effects predominantly originate from fluctuations of the order parameter, as originally proposed in the seminal work of Ref. [34]. Additionally, our findings directly map the impact of the intercalation-induced disorder, which concerns both the dc transport data as well as the optical outcome at any FIR-MIR energy scales (Fig. 2). In this context, alternative avenues may be considered for the interplay between the CDW transition and disorder itself. It is worth recalling the setting based on the excitonic insulator dynamics [35,36], which was advanced as major ingredient for the (Overhauser-type) CDW state in $\mathrm{TiSe_2}$ [37]. In fact, Cu intercalation in $\mathrm{TiSe_2}$ suppresses such excitonic correlations, leaving, nonetheless, the electron-phonon interaction less affected and thus allowing the presence of CDW incommensurations [6,7]. Whether this is likely pertinent for our materials calls for further investigations. As a matter of fact, contrary to the semimetallic nature of the CDW state in $1T$-TiSe$_2$, the shape of FS in ErTe$_3$, evinced from the angle-resolved-photoemission-spectroscopy [38], principally tends to favor the creation of CDW gaps by perpendicular FS nesting vectors. Raman data, though, question the nesting as a unique driving mechanism for the CDW transition; instead of a purely electronic instability, the CDW ordering vector could be determined by a lattice distortion driven by some other mechanism exploiting the role of the electron-phonon coupling in the spirit of a so-called focusing effect [20]. Generally, solving the dichotomy about the repercussion of disorder on the CDW collective state would also be instrumental towards superconductivity, as we now cursorily flash.

As a future outlook, it indeed remains to be seen how the gradual suppression of the CDW state and of its anisotropic character with disorder, as disclosed by our optical data, paves the way to the onset of superconductivity upon Pd intercalation. Since T_c in Pd$_x$ErTe$_3$ typically does not exceed 3 K, our optical tool must be complemented with resonant-cavity investigations to achieve the expected, relevant energy scales of the superconducting state. Nonetheless and even though superconductivity appears at Pd-intercalations $x > 2\%$ [8], upon extrapolating our results for $x \leqslant 1.2\%$ we might be tempted to suggest that electrons involved in the superconducting pairing instead of competing for the same portions of FS do actually coexist with those of the CDW segments [15,30] and that superconductivity generically bunches out from a pseudogaplike phase, as for HTC [1]. The suppression of the electronic anisotropy upon Pd intercalation in ErTe$_3$ concomitant with the onset of superconductivity may equally resemble the situation at the intertwined nematic, CDW, and superconducting order, lately considered to be an ubiquitous feature in unconventional superconductors (like in iron-based and kagome materials) [39–41]. Lastly, enlightening how our results could be compatible with the suggestive Bragg glass phase at weak disorder (i.e., the regime addressed here), as alluded by the scanning tunneling microscopy data [9], still needs to be addressed and would furthermore profit from the support of dedicated theoretical work.

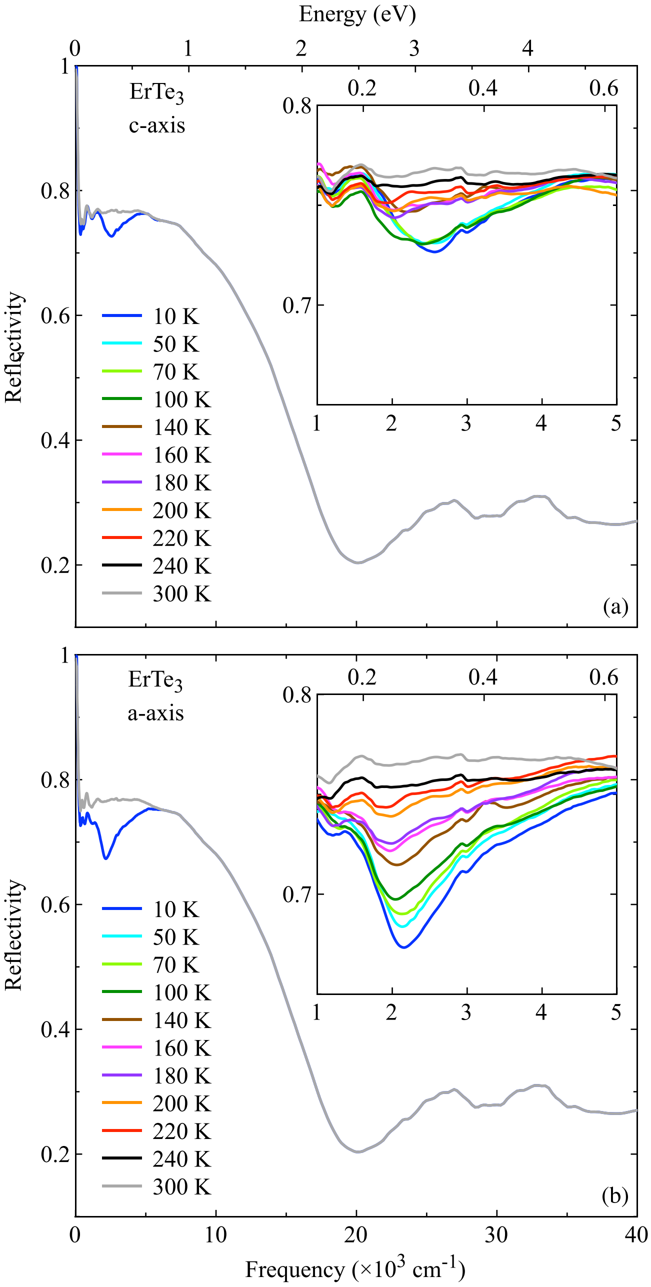

FIG. 5. $R(\omega)$ along the c (a) and a (b) axes [Fig. 4(a)] of ErTe$_3$ at 300 and 10 K ($1\,\text{eV} = 8.06548 \times 10^3\ \text{cm}^{-1}$), emphasizing the plasma edge feature and the high-frequency spectrum. The insets show the corresponding T dependence at MIR energy scales.

ACKNOWLEDGMENT

Work at Stanford was supported by the Department of Energy, Office of Basic Energy Sciences under Contract No. DE-AC02-76SF00515.

APPENDIX

1. Samples, experimental techniques, and data

a. Samples characterization and crystal structure

The chemical analysis of our samples was performed in a JEOL JXA-8230 SuperProbe electron microprobe system, calibrated to ErTe$_3$ and PdTe$_2$ secondary standards [8]. The microprobe analysis showed that ∼12% of the Pd present in the melt were incorporated into the crystals during growth and that the crystal composition is uniform to within experimental error at different spots on a crystal surface and between crystals grown in the same batch. Plate-shaped crystals [b axis normal to the ac plane, Fig. 4(a)] 1–3 mm across were routinely produced. The crystal plate area remained fairly constant, but the resulting thicknesses decreased as Pd concentration (x) increased, from several hundred microns for $x = 0$ to approximately 50 microns for $x = 0.05$ Pd-intercalated ErTe$_3$. This offers indirect evidence that Pd atoms act as intercalants between the Te planes, in that their presence tends to disrupt and slow the rate of growth in this direction [8].

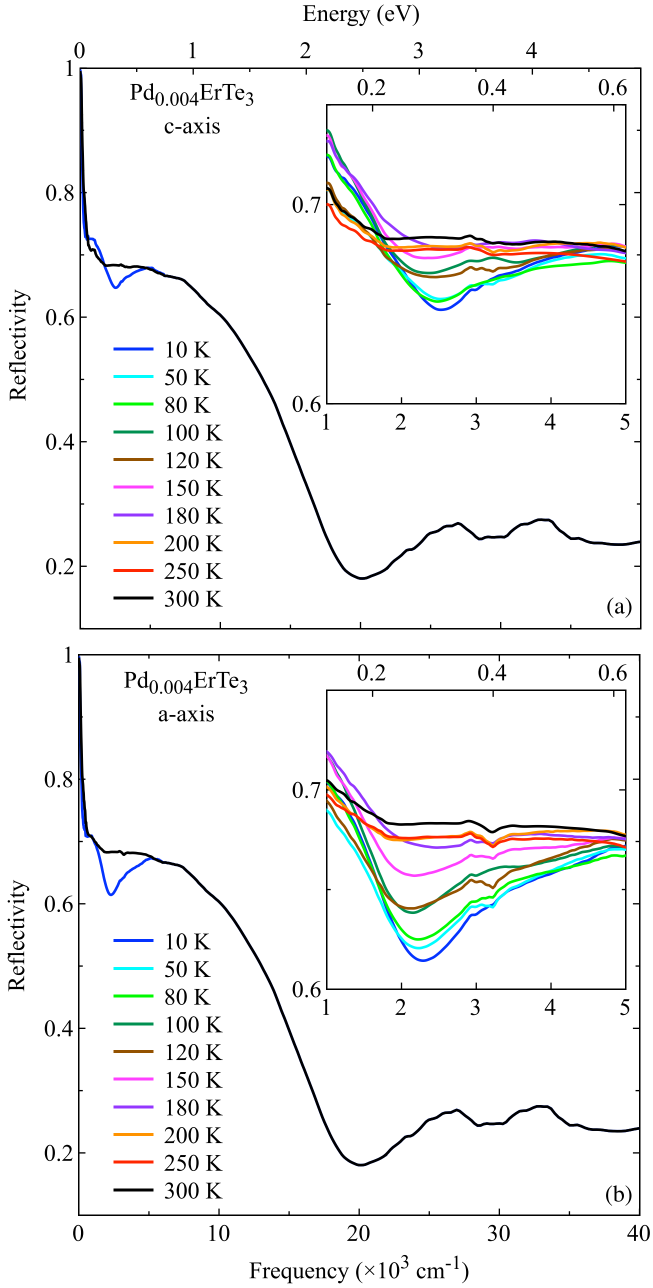

FIG. 6. $R(\omega)$ along the c (a) and a (b) axes [Fig. 4(a)] of $x = 0.004$ Pd$_x$ErTe$_3$ at 300 and 10 K (1 eV = 8.06548×10^3 cm^{-1}), emphasizing the plasma edge feature and the high-frequency spectrum. The insets show the corresponding T dependence at MIR energy scales.

The crystal structure [Fig. 4(a)] is formed by alternating puckered RTe slabs with bilayers of approximately square nets of Te atoms. The presence of a glide plane in the stacking of these layers creates a 0.05% [14] difference between the in-plane a and c axes lattice parameters at 300 K and biases the primary CDW transition to order along the c axis. The space group of RTe$_3$ is nominally orthorhombic ($Cmcm$), even though evidence for effectively fourfold symmetric electronic properties were pointed out in the literature [8].

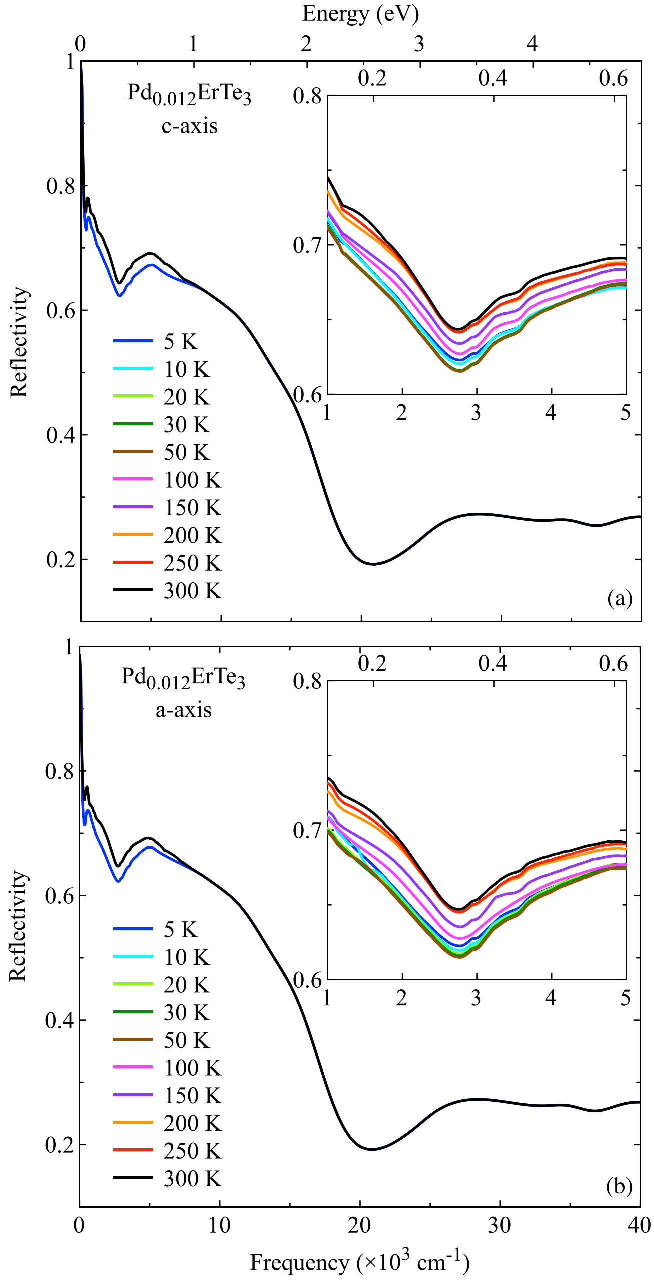

FIG. 7. $R(\omega)$ along the c (a) and a (b) axes [Fig. 4(a)] of $x = 0.012$ Pd$_x$ErTe$_3$ at 300 and 5 K (1 eV = 8.06548×10^3 cm^{-1}), emphasizing the plasma edge feature and the high-frequency spectrum. The insets show the corresponding T dependence at MIR energy scales.

b. dc transport characterization

Measurements of the T dependence of the resistance were performed in a Janis Supertran-VP continuous flow cryostat. The resistivity in the ac plane [Fig. 4(a)] was measured on thin rectangular crystals which had been cut with a scalpel and cleaved to expose a clean surface immediately before contacting. Crystals were cut such that current flows along the (101) axis, and contacts were attached to the surface in the transverse geometry [16]. In this geometry, the sum of the resistivity components along the crystal axes $\rho^a_{\mathrm{dc}} + \rho^c_{\mathrm{dc}}$

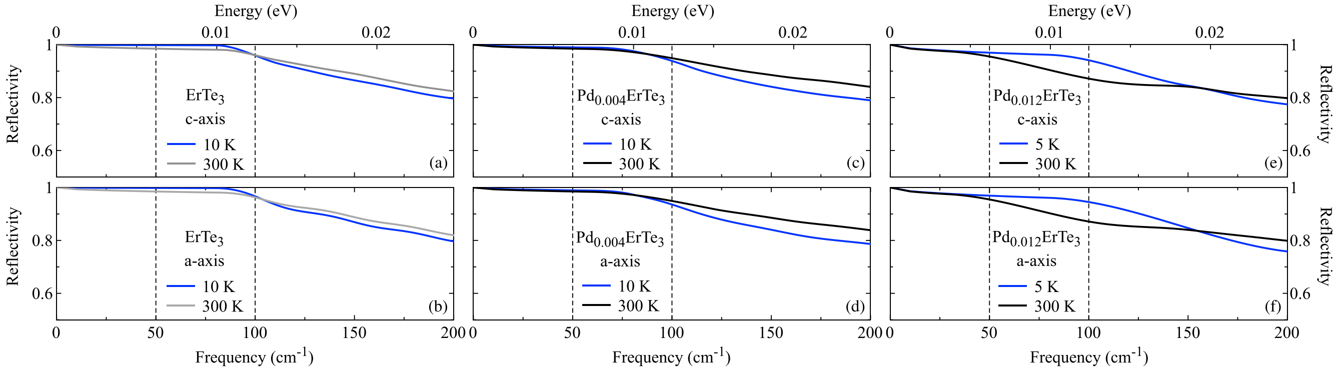

FIG. 8. Low frequency $R(\omega)$ at 300 and 5 or 10 K for both a and c axes [Fig. 4(a)] at the smooth crossover between the measured data in FIR and the HR extrapolation: (a), (b) $x = 0$; (c), (d) $x = 0.004$; and (e), (f) $x = 0.012$ $\mathrm{Pd}_x\mathrm{ErTe}_3$. The vertical dashed lines indicate the energy interval between 50 and 100 cm^{-1}, where the numerical interpolation of data and HR extrapolation takes place.

and the in-plane resistivity anisotropy $\rho^a_{\mathrm{dc}} - \rho^c_{\mathrm{dc}}$ are measured simultaneously within the same crystal [8,16]. The extracted ρ^a_{dc} and ρ^c_{dc} are displayed in Figs. 4(b)–4(d) for compositions coinciding or very close to the Pd intercalations investigated in our paper. One can easily recognize the two consecutive CDW transitions (at least at low Pd intercalations) with bumplike features and/or changes of slope at T_{CDW1} and T_{CDW2} [dashed lines in Figs. 4(b)–4(d)], which lower with increasing Pd intercalation. The dc anisotropy, shown in Fig. 2, derives from these data in Figs. 4(b)–4(d), thus comparing our samples with $x = 0.004$ and 0.012 Pd intercalation to the $x = 0.005$ and 0.019 compositions, respectively.

It has been broadly established that T_{CDW1} marks the onset of the primary CDW order, while T_{CDW2} of the second, orthogonal CDW component. Thus, despite the nearly tetragonal symmetry of the crystal, the phase at $T_{\mathrm{CDW2}} < T < T_{\mathrm{CDW1}}$ has unidirectional CDW order, while the low-temperature phase is bidirectional, but with generally inequivalent strengths. The two CDW transitions in ErTe_3 are associated with nesting wave vectors $q_{\mathrm{CDW1}} \simeq 0.7c^*$ and $q_{\mathrm{CDW2}} \simeq 0.68a^*$ (with $a^* = 2\pi/a_0$ and $c^* = 2\pi/c_0$; a_0 and c_0 are the respective in-plane lattice constants) [15].

c. Measured optical reflectivity

Figures 5–7 display the measured T dependence of the in-plane optical reflectivity [$R(\omega)$] for all investigated compounds along the c and a axes [Fig. 4(a)]. In all data sets, we recognize the typical metallic behavior with a T-independent plasma edge [i.e., sharp increase of $R(\omega)$ upon decreasing frequency], having its onset at approximately 2×10^4 cm^{-1}. While the T dependence of $R(\omega)$ mainly occurs at MIR frequencies for all Pd intercalations (insets in Figs. 5–7), the anisotropy of the optical response appears in an obvious fashion at low x but is quite negligible for the $x = 0.012$ Pd intercalation. There is a fair agreement with previously collected (unpolarized) data [21,22], even though the overall $R(\omega)$ magnitude is here sensibly lower. This might be due to some scattering because of not perfectly flat surfaces after the fresh cleaving, which was performed prior to each measurement. This should not impede a trusty outcome of our analysis, since we are mainly interested in quantities representing either the optical anisotropy or the relative T dependence, thus based on their ratio between both polarizations or on normalized ones with respect to 300 K for each axis (Figs. 1–3), respectively. We also note that these data as well as our earlier unpolarized ones in ErTe_3 [21] do not reveal a second deep in $R(\omega)$ around 800 cm^{-1} at $T \ll T_{\mathrm{CDW2}}$ either (also true for Pd-intercalated compounds), in contrast to previous claims [22]. We tend to exclude major sample issues related to their growth procedure or their degradation but speculate that, if real, the resulting additional absorption feature in Ref. [22], yet distinct from our low-frequency shoulder at the MIR peak (see insets of Fig. 1 and below Figs. 9–11), might be overcast by the metallic contribution in our samples.

d. Optical conductivity and integrated spectral weight

The real part [$\sigma_1(\omega)$] of the optical conductivity is then achieved via the Kramers-Kronig transformation of the measured $R(\omega)$. To this goal, appropriate extrapolations of $R(\omega)$ are performed for $\omega \to 0$ and ∞. Below the lowest measured frequency, the Hagen-Rubens (HR) relation [$R(\omega) = 1 - 2\sqrt{\frac{\omega}{\sigma_{dc}}}$] for a metal is used. The values for the dc conductivity (σ_{dc}) satisfy the relative T dependence of $\rho_{\mathrm{dc}}(T)$ [Figs. 4(b)–4(d)]. The interpolation between the HR extrapolation and the measured data in FIR, performed within an energy interval between 50 and 100 cm^{-1}, follows a standard, common procedure and allows us to smoothly connect them, as shown explicitly in Fig. 8. Above the highest measured frequency, $R(\omega)$ is first assumed to be constant up to 7 eV and above $R(\omega)$ is set to be consistent with the free-electron response ($\propto \omega^{-4}$) [17].

Figures 9–11 collect the derived T dependence of the in-plane $\sigma_1(\omega)$, highlighting the spectral range below 10^4 cm^{-1}. The optical anisotropy between the c and a axes and its intercalation dependence as anticipated above for $R(\omega)$ are equally reproduced in $\sigma_1(\omega)$. As also shown in the corresponding insets, there are two relevant features in the spectra: a zero-energy mode, ascribed to the metallic Drude resonance, and a strong MIR absorption. The metallic component gets narrow with decreasing T at low Pd intercalations but broadens substantially for $x = 0.012$ $\mathrm{Pd}_x\mathrm{ErTe}_3$. The Drude resonance and the MIR absorption are very distinct at all T and can also be recognized in earlier work [21,22], yet more blurred upon increasing T. In fact, the MIR absorption was identified

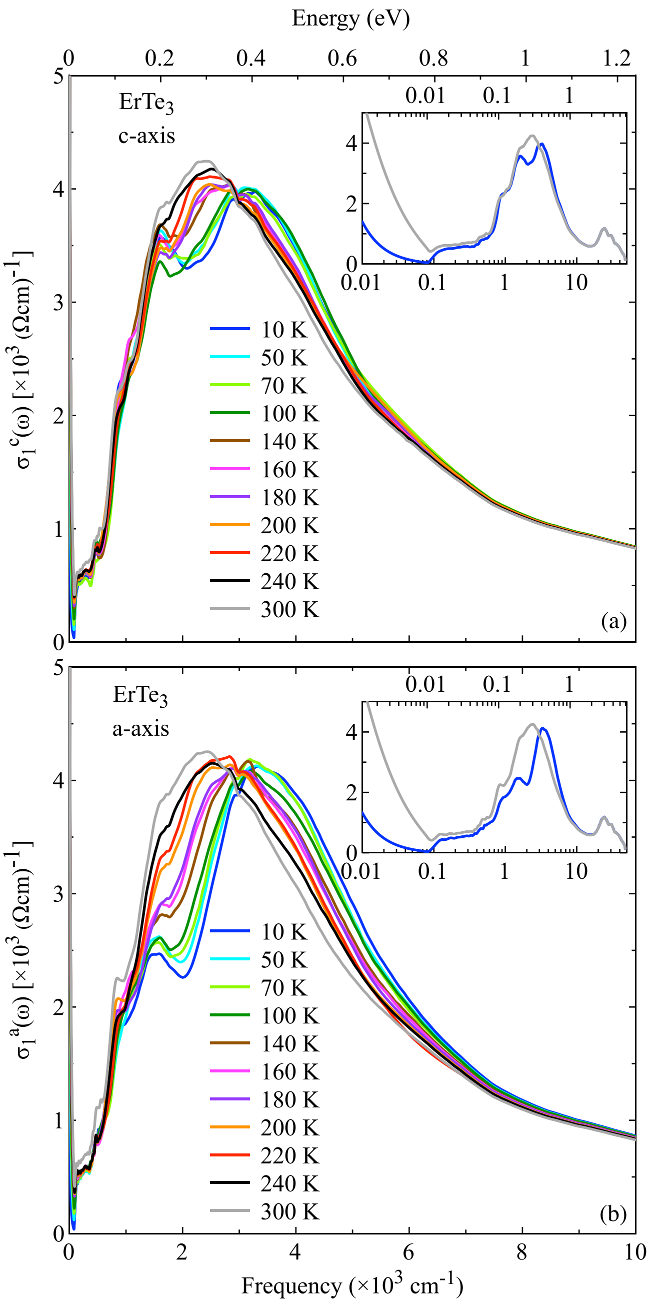

FIG. 9. T dependence of $\sigma_1(\omega)$ along the c (a) and a (b) axes [Fig. 4(a)] of ErTe$_3$ (1 eV $= 8.06548 \times 10^3$ cm^{-1}), emphasizing the MIR-NIR spectral range. The insets show the corresponding spectra at 300 and 10 K over the whole investigated spectral range (please note the logarithmic frequency (energy) scale).

as a very broad feature at high T, almost disappearing into the large high frequency Drude tail [21]. The peculiar T dependence of the strong MIR absorption is then of interest. As emphasized by the main panels in Fig. 9, that MIR absorption in ErTe$_3$ consists of a peak with a shoulder on its low-frequency side at high T, crossing over into two distinct peaks at low T. Such a behavior is still observable in the $x = 0.004$ Pd intercalation (Fig. 10), while the low frequency shoulder of the MIR peak for the $x = 0.012$ Pd intercalation remarkably broadens upon lowering T (Fig. 11).

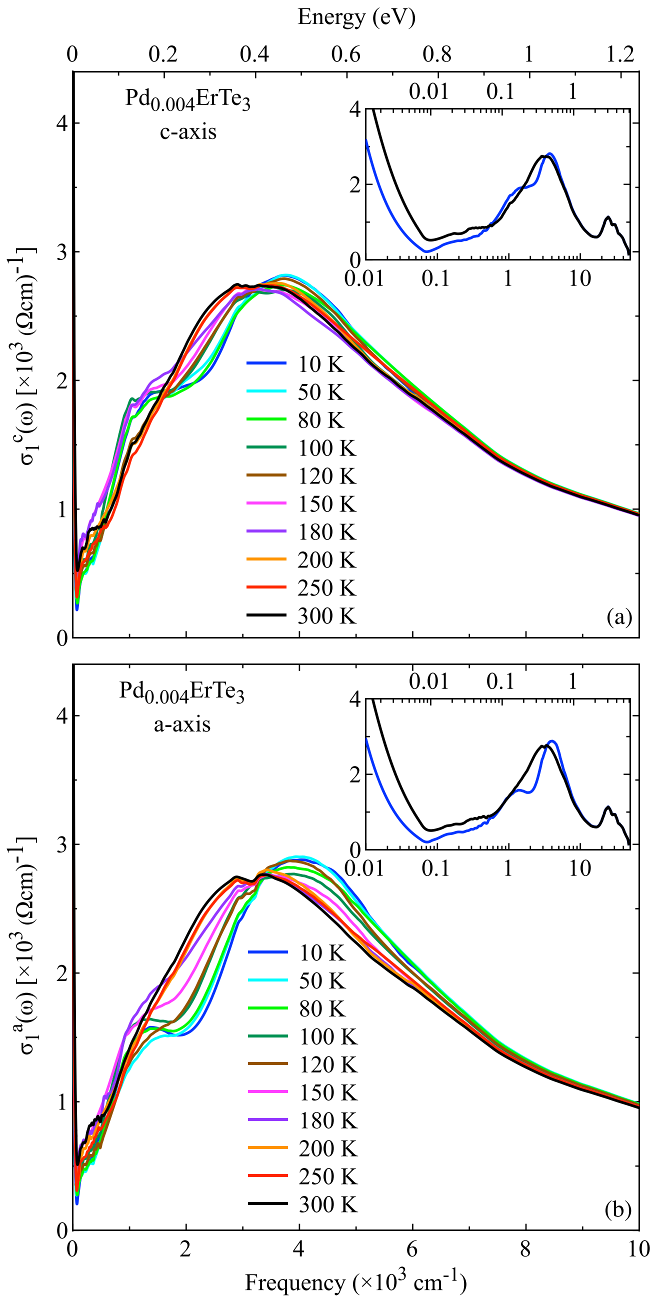

FIG. 10. T dependence of $\sigma_1(\omega)$ along the c (a) and a (b) axes [Fig. 4(a)] of $x = 0.004$ Pd$_x$ErTe$_3$ (1 eV $= 8.06548 \times 10^3$ cm^{-1}), emphasizing the MIR-NIR spectral range. The insets show the corresponding spectra at 300 and 10 K over the whole investigated spectral range (please note the logarithmic frequency (energy) scale).

A quite central quantity in our discussion is the spectral weight (SW) and its distribution [26]. SW is generically defined through the direct integration of $\sigma_1(\omega)$ in chosen energy intervals between ω_i ($i = 1$ and 2) so that $\mathrm{SW}(T) = \frac{Z_0}{\pi^2}\int_{\omega_1}^{\omega_2}\sigma_1(\omega';T)d\omega'$ (i.e., expressed in units of cm^{-2} and with $Z_0 = 376.73\ \Omega$ being the impedance of free space). This model-independent quantity is related to the number of effective carriers (normalized by their effective mass) contributing to the optical processes within the integration limits and reflects the evolution of the electronic band structure upon

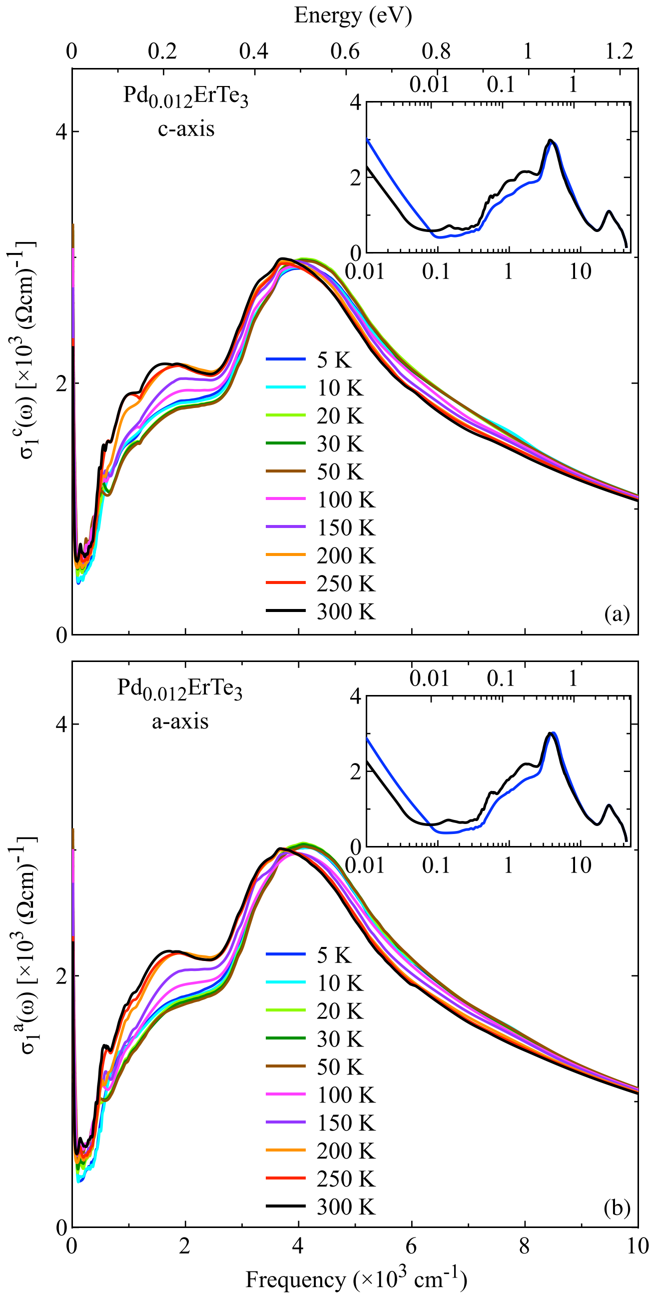

FIG. 11. T dependence of $\sigma_1(\omega)$ along the c (a) and a (b) axes [Fig. 4(a)] of $x = 0.012$ Pd$_x$ErTe$_3$ ($1\,\text{eV} = 8.06548 \times 10^3\ \text{cm}^{-1}$), emphasizing the MIR-NIR spectral range. The insets show the corresponding spectra at 300 and 5 K over the whole investigated spectral range (please note the logarithmic frequency (energy) scale).

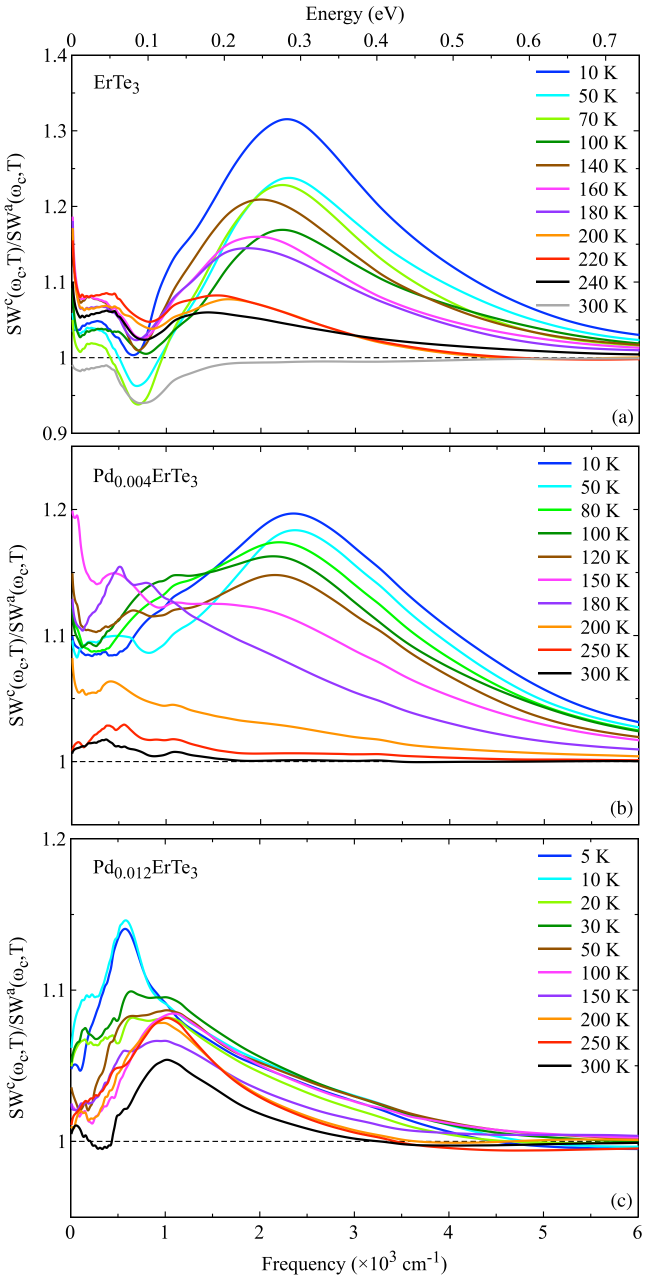

FIG. 12. T dependence of the ratio SW$^c(\omega_c, T)$/SW$^a(\omega_c, T)$ for the integrated SW (insets Fig. 3) as a function of the cutoff frequency ω_c (see text) at selected T for $x = 0$ (a), $x = 0.004$ (b), and $x = 0.012$ (c) Pd$_x$ErTe$_3$ ($1\,\text{eV} = 8.06548 \times 10^3\ \text{cm}^{-1}$).

varying T. In the case $\omega_1 = 0$ and for the $\omega_2 \to \infty$ limit, the resulting integrated SW(T) is expected to merge to a constant value at all T, satisfying the optical f-sum rule [17]. The integrated SW $\sim \int_0^{\omega_c} \sigma_1(\omega) d\omega$ is here fully recovered at energy scales (ω_c) above 10^4 cm^{-1} and its reshuffling mainly occurs at MIR frequencies at all T. Before going any further, it is worth recalling that if there is a transfer of SW from high to low energies, the SW ratio (i.e., SW$^{c,a}(T)$/SW$^{c,a}(300\,\text{K})$, shown in Fig. 3) will exceed 1 at low energies and then smoothly approach 1 upon increasing frequency until the full energy scale of the low-energy resonance is reached. For instance, SW may move into the metallic (Drude) zero-energy mode. If there is a transfer of SW from low to high energies though, the SW ratio will fall below 1 until the energy scale of the total SW transfer is accomplished. This latter case may suggest some erosion of the density of states and a FS gapping, as it could step in by a reconstruction of the electronic band structure.

An alternative avenue is to focus on the SW anisotropy. Figure 12 indeed displays the ratio SW$^c(\omega_c, T)$/SW$^a(\omega_c, T)$ of the integrated spectral weight up to ω_c between the two relevant crystallographic axes, denoting an obvious deviation from the isotropic limit (i.e., ~ 1). That anisotropy (shown at selected ω_c in Fig. 2) smoothly evolves with lowering T but overall decreases in magnitude with Pd intercalation. As evidenced from other quantities [like, e.g., $\sigma_1(\omega)$], the affected spectral range tends to shift towards low-energy scales, concerning the FIR-MIR energy interval, upon Pd intercalation. All that testifies an anisotropic electronic band structure across and below E_F, coinciding with the CDW transitions.

2. Phenomenological data analysis

We fit the T dependence of the optical response using the phenomenological Drude-Lorentz approach, for which the dielectric function $\tilde{\varepsilon} = \varepsilon_1 + i\varepsilon_2$ is given by [17]

$$\tilde{\varepsilon}(\omega) = \varepsilon_\infty - \frac{\omega_{p,D}^2}{\omega^2 + \frac{i\omega}{\tau_D}} + \sum_j \frac{\Omega_j^2}{\omega_j^2 - \omega^2 - i\omega\gamma_j}, \tag{A1}$$

ε_∞ is the optical dielectric constant, which turns out in our fits to be close to 1 for all Pd$_x$ErTe$_3$. In the second term, $\Gamma_D = 1/\tau_D$ is the scattering rate and $\omega_{p,D}^2 = 4\pi ne^2/m^*$ is the squared plasma frequency for the itinerant (Drude) carriers, with n and m^* as the carrier concentration and effective mass, respectively. $\omega_{p,D}^2$ equally defines the so-called Drude weight. In the third term, ω_j, γ_j and Ω_j are the resonance frequency, width, and strength, respectively, of the jth Lorentz (Lj) harmonic oscillators (HOs), which describe bound excitations. The square of their strength (Ω_j^2) corresponds to the SW encountered in each Lj excitation. The use of the Drude and Lj-HOs SW is obviously an alternative approach to the direct integration of the measured quantity $\sigma_1(\omega)$, as introduced above and elaborated upon in the main text. However, below we will return to a comparison between the two methods, pointing out their mutual consistency and complementarity.

The real part $\sigma_1(\omega)$ of the optical conductivity is specifically at the center of our analysis, for which we seek a series of additive components being equivalent for all Pd intercalations and for both polarization directions. It turns out that a reliable fit covering the whole measured spectral range consists of one Drude term and six HOs. Figures 13–15 display the T dependence of the Drude as well as of the Lj-HOs parameters, while the panels of the right column in Figs. 16 and 17 visualize the fit components across the spectral range of interest along both the a and c axes. The same fit philosophy, which nonetheless copies rather well a previous analysis for unpolarized data on ErTe$_3$ [21], allows a fairly precise reproduction of the spectra at any T and polarization directions for all Pd intercalations, thus supporting a comprehensive and consequent discussion even beyond the intrinsic model-dependent nature of this phenomenological approach.

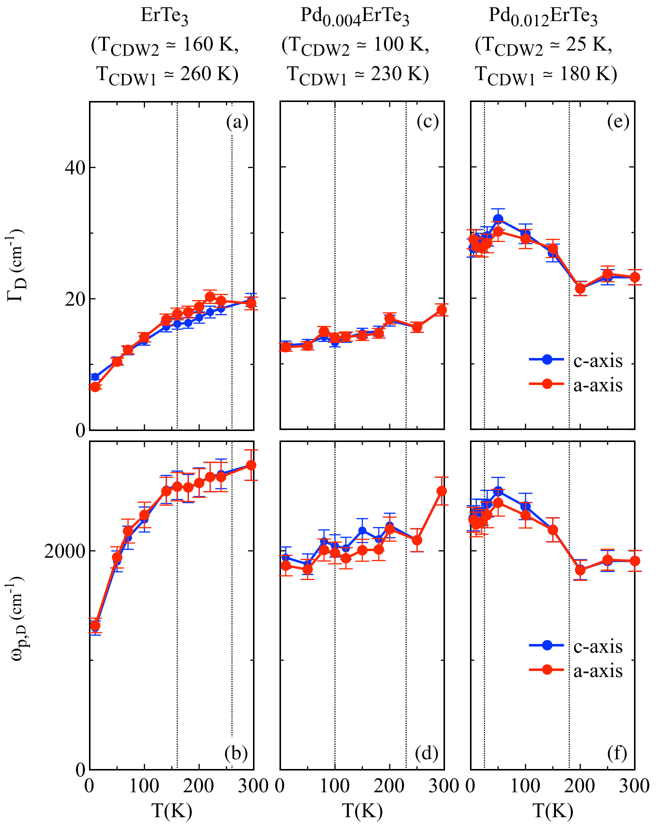

FIG. 13. T dependence of the Drude scattering rate Γ_D (upper panels) and plasma frequency $\omega_{p,D}$ (lower panels) fit parameters [Eq. (A1)] for all Pd$_x$ErTe$_3$ along the c and a axes: (a), (b) $x = 0$; (c), (d) $x = 0.004$; and (e), (f) $x = 0.012$. The vertical dotted lines mark T_{CDW1} and T_{CDW2} [8,16]. The error bars are estimated numerically within the nonlinear least-squares fit technique.

We first comment on the fit parameters of the Drude term. Both the $x = 0$ and 0.004 Pd intercalations display a monotonous decrease of the scattering rates and plasma frequencies with decreasing T [Figs. 13(a)–13(d)]. The T dependence of Γ_D indicates a typical, effective metallic behavior, while that of $\omega_{p,D}$ suggests an erosion of the metallic SW which gets quite pronounced for $x = 0$ at low T. These trends are again an indication for a progressively enhanced gapping of FS because of the CDW transitions (see an alternative elaboration around Fig. 3), similarly accompanied by a reduction of available scattering channels. Somehow opposite is the situation for the $x = 0.012$ Pd intercalation, since both Drude parameters increase upon lowering T below T_{CDW1} prior to being weakly depleted at the lowest measured T below T_{CDW2} [Figs. 13(e) and 13(f)]. Therefore, only at the lowest T can an effective but still partial gapping of FS and a modest switching-off of scattering channels be optically mirrored as a consequence of the CDW transitions. Otherwise, disorder by Pd intercalation seems here to dominate at T between the two CDW transitions, with increasing scattering. This is then compensated by an increasing Drude plasma frequency for $T_{\text{CDW2}} < T < T_{\text{CDW1}}$, denoting some enhancement of FS with more itinerant, yet less mobile charge carriers due to impurity bands. All in all, this may presage a nearly saturated T dependence of $\rho_{\text{dc}}(T)$ for both in-plane axes besides the broad, humble anomaly below T_{CDW1}, as observed, for instance, in the $x = 0.019$ composition [Fig. 4(d)]. At this stage, it is worth warning the readers that it is admittedly challenging to perform a unique as well as fully reliable fit of the zero-energy resonance, since such an effective metallic component of $\sigma_1(\omega)$ is very narrow and at low T even quite resolution-limited (i.e., almost fully beyond the measured experimental spectral range). Therefore, despite the

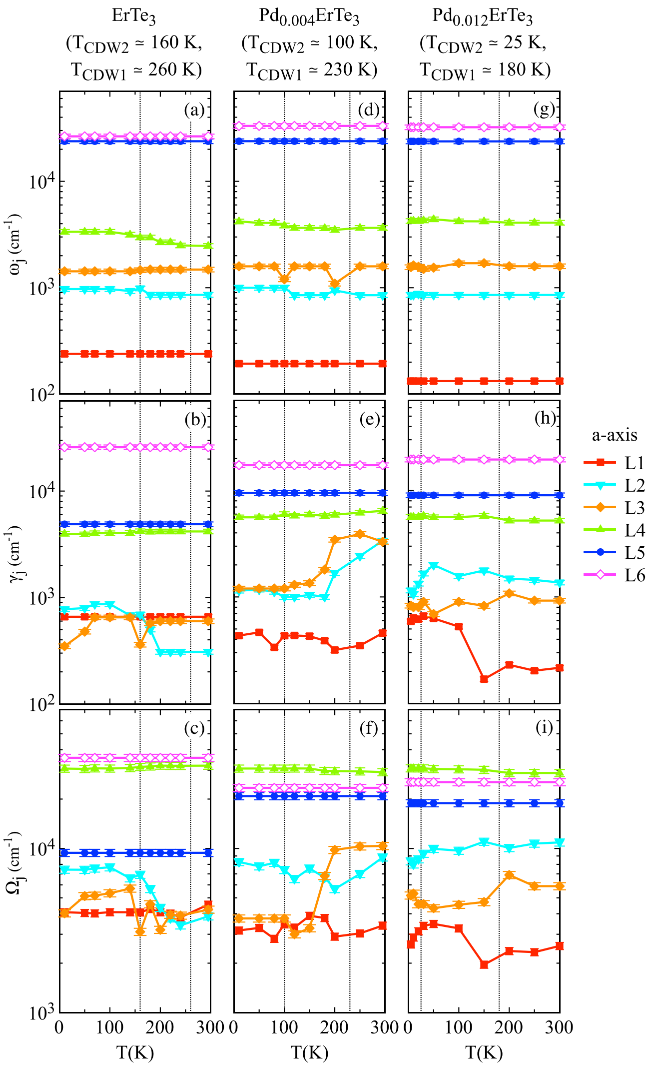

FIG. 14. T dependence of the Lj-HOs resonance frequency ω_j (upper panels), damping γ_j (middle panels), and strength Ω_j (lower panels) fit parameters [Eq. (A1)] for all Pd$_x$ErTe$_3$ along the a axis: (a)–(c) $x = 0$, (d)–(f) $x = 0.004$; and (g)–(i) $x = 0.012$. The vertical dotted lines mark T_{CDW1} and T_{CDW2} [8,16]. The error bars are estimated numerically within the nonlinear least-squares fit technique.

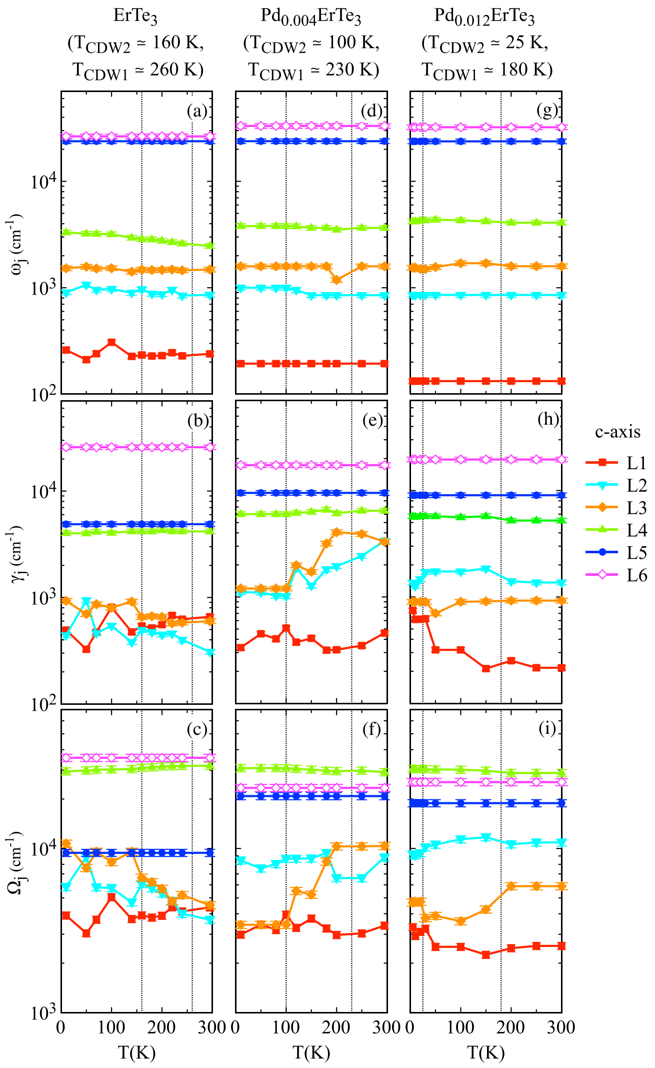

FIG. 15. T dependence of the Lj-HOs resonance frequency ω_j (upper panels), damping γ_j (middle panels), and strength Ω_j (lower panels) fit parameters [Eq. (A1)] for all Pd$_x$ErTe$_3$ along the c axis: (a)–(c) $x = 0$; (d)–(f) $x = 0.004$; and (g)–(i) $x = 0.012$. The vertical dotted lines mark T_{CDW1} and T_{CDW2} [8,16]. The error bars are estimated numerically within the nonlinear least-squares fit technique.

fair qualitative agreement between the measured dc transport properties and their anisotropy and the calculated one from the Drude model, there is no pretension about any quantitative conclusions. However, as addressed below in terms of the encountered SW, the metallic spectral range in $\sigma_1(\omega)$ plays a marginal role with respect to the FIR-MIR energy interval.

As far as the fit parameters of HOs are concerned, we remark on an almost monotonous T dependence, with some exceptions (Figs. 14 and 15): HOs L5 and L6 turn out to be fully T independent and specifically HOs L1 to L3 show some abrupt or sudden changes in T, particularly for their damping and strength, when crossing either CDW transition. This means that the CDW transitions do not only affect the bands crossing E_F and, consequently, the Drude fit parameters (Fig. 13), but also those bands deep into the electronic structure (i.e., far from E_F), suggesting its (intercalation-driven) remodeling. This is addressed next from the perspective of the SW redistribution.

Complementary to our analysis of the integrated SW in the main text, we can now single out the relevant spectral ranges harboring the T-dependent SW reshuffling. The fit components themselves, for which SW $\sim \omega_{p,D}^2$ (Drude) and SW $\sim \Omega_j^2$ (Lorentz Lj-HO), identify the selected spectral ranges. We state the redistribution of SW as its relative change with respect to 300 K, i.e., $\Delta\mathrm{SW}(T) = \mathrm{SW}(T) - \mathrm{SW}(300\ \mathrm{K})$ (Figs. 16 and 17 for the a and c axes, respectively). For the $x = 0$ and 0.004 Pd intercalations and along both axes [Figs. 16(a), 16(c), 17(a), and 17(c)], there is a weak depletion of SW upon lowering T related to the Drude term [as anticipated above when presenting Figs. 13(b) and 13(d)] and its high-frequency tail incorporated by HO L1 (i.e., Drude + L1 in Figs. 16(a), 16(c), 17(a), and 17(c) refers to SW $\sim \omega_{p,D}^2 +$

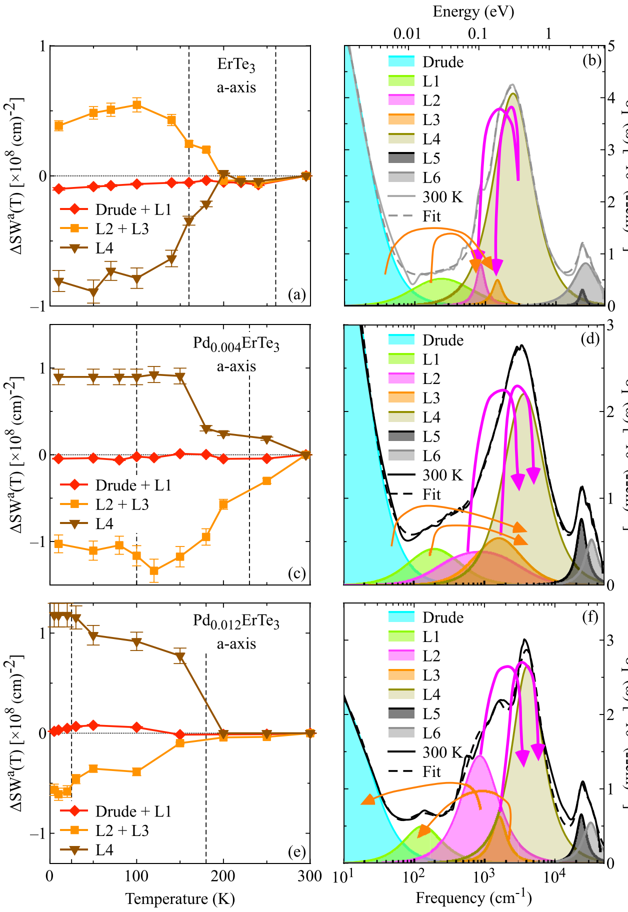

FIG. 16. Left column: T dependence of the spectral weight relative variation $\Delta\mathrm{SW}(T) = \mathrm{SW}(T) - \mathrm{SW}(300\ \mathrm{K})$, calculated for the grouped contributions given by the Drude term and HO L1 (i.e., $\mathrm{SW} \sim \omega_{p,D}^2 + \Omega_1^2$), by HOs L2 and L3 (i.e., $\mathrm{SW} \sim \Omega_2^2 + \Omega_3^2$), as well as by HO L4 (i.e., $\mathrm{SW} \sim \Omega_4^2$) with respect to 300 K. The error bars in $\Delta\mathrm{SW}(T)$ correspond to the direct propagation of the error in the HOs strength, estimated numerically within the nonlinear least-squares fit technique. Right column: $\sigma_1(\omega)$ at 300 K compared to its Drude-Lorentz fit [Eq. (A1)], showing its single constituent components (please note the logarithmic frequency (energy) scale). The rounded arrows mimic the direction of the SW reshuffling upon decreasing T, which is stronger with thicker arrows. All quantities are shown along the a axis [Fig. 4(a)] for all Pd$_x$ErTe$_3$: (a), (b) $x = 0$; (c), (d) $x = 0.004$; and (e), (f) $x = 0.012$. The vertical dashed lines in (a), (c), and (e) mark T_{CDW1} and T_{CDW2} [8,16].

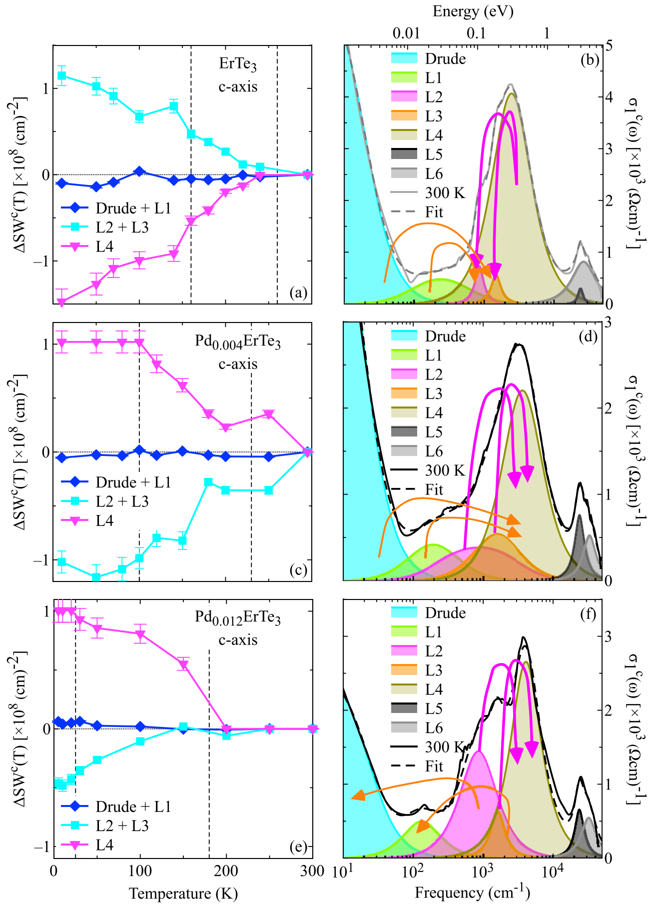

FIG. 17. Left column: T dependence of the spectral weight relative variation $\Delta\mathrm{SW}(T) = \mathrm{SW}(T) - \mathrm{SW}(300\ \mathrm{K})$, calculated for the grouped contributions given by the Drude term and HO L1 (i.e., $\mathrm{SW} \sim \omega_{p,D}^2 + \Omega_1^2$), by HOs L2 and L3 (i.e., $\mathrm{SW} \sim \Omega_2^2 + \Omega_3^2$), as well as by HO L4 (i.e., $\mathrm{SW} \sim \Omega_4^2$) with respect to 300 K. The error bars in $\Delta\mathrm{SW}(T)$ correspond to the direct propagation of the error in the HOs strength, estimated numerically within the nonlinear least-squares fit technique. Right column: $\sigma_1(\omega)$ at 300 K compared to its Drude-Lorentz fit [Eq. (A1)], showing its single constituent components [please note the logarithmic frequency (energy) scale]. The rounded arrows mimic the direction of the SW reshuffling upon decreasing T, which is stronger with thicker arrows. All quantities are shown along the c axis [Fig. 4(a)] for all Pd$_x$ErTe$_3$: (a), (b) $x = 0$; (c), (d) $x = 0.004$; and (e), (f) $x = 0.012$. The vertical dashed lines in (a), (c), and (e) mark T_{CDW1} and T_{CDW2} [8,16].

Ω_1^2). The $x = 0.012$ Pd intercalation, though, is at variance. As already said in relation to Fig. 13(f) and for both axes, some very moderate SW first moves to the Drude term and its tail represented by HO L1 with decreasing T but then below T_{CDW2}, a renewed and weak SW suppression takes place at the metallic components. It is striking that the damping and partially the strength of HO L1 for the $x = 0.012$ Pd intercalation are steadily enhanced for $T_{\mathrm{CDW2}} < T < T_{\mathrm{CDW1}}$, which could also mimic disorder-driven localization effects of the itinerant charge carriers [10], prior to the onset of the CDW condensate at $T < T_{\mathrm{CDW2}}$.

The moderate SW redistribution at low-energy scales for all Pd intercalations is accompanied by the stronger SW reshuffling pertinent to the spectral range covered by HOs L2 and L3 [i.e., L2 + L3 in Figs. 16(a), 16(c), 16(e), 17(a), 17(c), and 17(e)] refer to $\mathrm{SW} \sim \Omega_2^2 + \Omega_3^2$) as well as L4 (i.e., $\mathrm{SW} \sim \Omega_4^2$), and being similar along both axes. For $x = 0$, SW of HO L4 is removed and is then globally redistributed at low frequencies, accumulating into HOs L2 and L3 [Figs. 16(a) and 17(a)], when lowering T. Exactly the reverse behavior is observed for the $x = 0.004$ and 0.012 Pd intercalations [Figs. 16(c), 16(e), 17(c), and 17(e)]. In fact, SW along both axes accumulates into HO L4 at the partial costs of SW in HOs L2 and L3 at low T. Such trends upon lowering T seem to be initially rather gradual with a steady increase or depletion of ΔSW upon crossing T_{CDW1} and lean to a saturation of ΔSW below T_{CDW2} for all Pd intercalations. Interestingly enough, for the $x = 0$ and 0.004 Pd intercalations, the SW redistribution fully occurs within the indicated energy ranges related to each Lj-HOs and Drude term, since the involved total SW in the spectral range addressed here remains constant at any T (i.e., $\sum_i \Delta\mathrm{SW}_i \simeq 0$, with i running over each combination of the grouped fit components in Figs. 16 and 17 for both the a and c axes). On the contrary, for the $x = 0.012$ Pd intercalation, the SW reshuffling apparently does not guarantee its conservation at low T within the discussed spectral ranges for both axes; we may speculate that additional SW should move with decreasing T into the absorption described by HO L4 from excitations at higher energy scales and distributed over a large energy interval, eventually not accessible to our experiment.

Summarizing, the rounded arrows in Figs. 16(b), 16(d), 16(f), 17(b), 17(d), and 17(f) pictorially highlight the direction, and with increasing thickness catch a glimpse of the amount of the SW reshuffling upon decreasing T. This representation features the overall equivalent SW redistribution for both axes at each Pd intercalation. The metallic part (Drude) and its incoherent tail (HO L1) lose SW in favor of the low-frequency shoulder (HOs L2 and L3) of the MIR peak for the $x = 0$ and of the MIR peak itself (HO L4) for the $x = 0.004$ Pd-intercalation with decreasing T, respectively. On the other hand, that low-frequency shoulder (HOs L2 and L3) also profits and gets additionally reinforced from SW of the MIR peak (HO L4) in $x = 0$ but reversely loses SW towards the MIR peak for the $x = 0.004$ Pd intercalation upon lowering T. For the $x = 0.012$ Pd intercalation, the low-frequency shoulder (HOs L2 and L3) of the MIR peak experiences a diminishing SW at low T towards the metallic part of $\sigma_1(\omega)$ as well as towards the MIR peak (HO L4), contributing to its reinforcement. However, the major SW reshuffling when crossing the CDW transitions for all Pd intercalations effectively happens at and within the energy scales of the strong MIR peak in $\sigma_1(\omega)$, widely associated with the spectral range of the CDW gap(s) and spanned by the combination of the phenomenological HOs L2 to L4. Intriguingly enough, the SW reallocation along both axes at low T is towards the low-frequency tail of the MIR peak (i.e., from HO L4 to HOs L2 + L3) for the pristine materials, while it reinforces its high-frequency absorption (i.e., from HOs L2 + L3 to HO L4) as soon as Pd intercalation takes place.

---

[1] E. Fradkin, S. A. Kivelson, and J. M. Tranquada, Colloquium: Theory of intertwined orders in high temperature superconductors, Rev. Mod. Phys. **87**, 457 (2015), and references therein.

[2] P. W. Anderson, Absence of diffusion in certain random lattices, Phys. Rev. **109**, 1492 (1958).

[3] L. Li, X. Deng, Z. Wang, Y. Liu, M. Abeykoon, E. Dooryhee, A. Tomic, Y. Huang, J. B. Warren, E. S. Bozin, S. J. L. Billinge, Y. Sun, Y. Zhu, G. Kotliar, and C. Petrovic, Superconducting order from disorder in $2H$-TaSe$_{2-x}$S$_x$, npj Quantum Mater. **2**, 11 (2017).

[4] K. Cho, M. Kończykowski, S. Teknowijoyo, M. A. Tanatar, J. Guss, P. B. Gartin, J. M. Wilde, A. Kreyssig, R. J. McQueeney, A. I. Goldman, V. Mishra, P. J. Hirschfeld, and R. Prozorov, Using controlled disorder to probe the interplay between charge order and superconductivity in NbSe$_2$, Nat. Commun. **9**, 2796 (2018).

[5] E. Morosan, H. W. Zandbergen, B. S. Dennis, J. W. G. Bos, Y. Onose, T. Klimczuk, A. P. Ramirez, N. P. Ong, and R. J. Cava, Superconductivity in Cu$_x$TiSe$_2$, Nat. Phys. **2**, 544 (2006).

[6] D. Qian, D. Hsieh, L. Wray, E. Morosan, N. L. Wang, Y. Xia, R. J. Cava, and M. Z. Hasan, Emergence of Fermi Pockets in a New Excitonic Charge-Density-Wave Melted Superconductor, Phys. Rev. Lett. **98**, 117007 (2007).

[7] A. Kogar, G. A. de la Pena, S. Lee, Y. Fang, S. X.-L. Sun, D. B. Lioi, G. Karapetrov, K. D. Finkelstein, J. P. C. Ruff, P. Abbamonte, and S. Rosenkranz, Observation of a Charge Density Wave Incommensuration Near the Superconducting Dome in Cu$_x$TiSe$_2$, Phys. Rev. Lett. **118**, 027002 (2017).

[8] J. A. W. Straquadine, F. Weber, S. Rosenkranz, A. H. Said, and I. R. Fisher, Suppression of charge density wave order by disorder in Pd-intercalated ErTe$_3$, Phys. Rev. B **99**, 235138 (2019).

[9] A. Fang, J. A. W. Straquadine, I. R. Fisher, S. A. Kivelson, and A. Kapitulnik, Disorder-induced suppression of charge density wave order: STM study of Pd-intercalated ErTe$_3$, Phys. Rev. B **100**, 235446 (2019).

[10] Y. Huang, B. F. Hu, T. Dong, A. F. Fang, P. Zheng, and N. L. Wang, Effect of disorder in the charge-density-wave compounds LaTe$_{1.95}$ and CeTe$_{1.95-x}$Se$_x$ ($x = 0$ and 0.16) as revealed by optical spectroscopy, Phys. Rev. B **86**, 205123 (2012).

[11] For higher Pd concentrations, Te deficiencies might be present in Pd$_x$ErTe$_3$ [8], though for smaller Pd-intercalations this is not clear and Te vacancies are hardly detected.

[12] E. DiMasi, M. C. Aronson, J. F. Mansfield, B. Foran, and S. Lee, Chemical pressure and charge-density waves in rare-earth tritellurides, Phys. Rev. B **52**, 14516 (1995).

[13] N. Ru, J.-H. Chu, and I. R. Fisher, Magnetic properties of the charge density wave compounds RTe$_3$ (R = Y, La, Ce, Pr, Nd, Sm, Gd, Tb, Dy, Ho, Er, and Tm), Phys. Rev. B **78**, 012410 (2008).

[14] N. Ru, C. L. Condron, G. Y. Margulis, K. Y. Shin, J. Laverock, S. B. Dugdale, M. F. Toney, and I. R. Fisher, Effect of chemical pressure on the charge density wave transition in rare-earth tritellurides RTe$_3$, Phys. Rev. B **77**, 035114 (2008).

[15] A. Fang, A. G. Singh, J. A. W. Straquadine, I. R. Fisher, S. A. Kivelson, and A. Kapitulnik, Robust superconductivity intertwined with charge density wave and disorder in Pd-intercalated ErTe$_3$, Phys. Rev. Res. **2**, 043221 (2020).

[16] P. Walmsley and I. R. Fisher, Determination of the resistivity anisotropy of orthorhombic materials via transverse resistivity measurements, Rev. Sci. Instrum. **88**, 043901 (2017).

[17] M. Dressel and G. Gruner, *Electrodynamics of Solids* (Cambridge University Press, Cambridge, 2002).

[18] W. Kohn, Image of the Fermi Surface in the Vibration Spectrum of a Metal, Phys. Rev. Lett. **2**, 393 (1959).

[19] G. Grüner, *Density Waves in Solids*, Advanced Book Program: Addison-Wesley (Perseus Books Group, Reading, MA, 2000).

[20] H.-M. Eiter, M. Lavagnini, R. Hackl, E. A. Nowadnick, A. F. Kemper, T. P. Devereaux, J.-H. Chu, J. G. Analytis, I. R. Fisher, and L. Degiorgi, Alternative route to charge density wave formation in multiband systems, Proc. Natl. Acad. Sci. **110**, 64 (2013).

[21] F. Pfuner, P. Lerch, J.-H. Chu, H.-H. Kuo, I. R. Fisher, and L. Degiorgi, Temperature dependence of the excitation spectrum in the charge-density-wave $ErTe_3$ and $HoTe_3$ systems, Phys. Rev. B **81**, 195110 (2010).

[22] B. F. Hu, B. Cheng, R. H. Yuan, T. Dong, A. F. Fang, W. T. Guo, Z. G. Chen, P. Zheng, Y. G. Shi, and N. L. Wang, Optical study of the multiple charge-density-wave transitions in $ErTe_3$, Phys. Rev. B **84**, 155132 (2011).

[23] N. Ru and I. R. Fisher, Thermodynamic and transport properties of YTe_3, $LaTe_3$, and $CeTe_3$, Phys. Rev. B **73**, 033101 (2006).

[24] B. F. Hu, B. Cheng, R. H. Yuan, T. Dong, and N. L. Wang, Coexistence and competition of multiple charge-density-wave orders in rare-earth tritellurides, Phys. Rev. B **90**, 085105 (2014).

[25] The dc anisotropy is evinced from the resistivity data available in the literature [8,16] and reproduced in Figs. 4(b)–4(d) of the Appendix for compositions coinciding or close enough to the Pd intercalations investigated in this paper.

[26] The spectral weight (SW) of the optical conductivity corresponds to its integral $\mathrm{SW}(T) = \frac{Z_0}{\pi^2}\int_0^{\omega_c}\sigma_1(\omega';T)d\omega'$, expressed in units of cm^{-2} ($Z_0 = 376.73\Omega$, being the impedance of free space) [17]. ω_c is the cutoff energy. See Appendix for further details.

[27] N. P. Ong and P. Monceau, Anomalous transport properties of a linear-chain metal: $NbSe_3$, Phys. Rev. B **16**, 3443 (1977).

[28] The estimation of the FS gapping from $\rho_{\mathrm{dc}}(T)$ is calculated with the formula $[(\sigma_{\mathrm{norm}} - \sigma_{\mathrm{peak}})/\sigma_{\mathrm{norm}}]$, where σ_{peak} is the dc conductivity at its anomaly minimum at T_{peak} (i.e., T_{peak} is the temperature at which incidentally $\rho_{\mathrm{dc}}(T)$ displays the bump-like maximum) and σ_{norm} is its expected normal value without anomaly at the same T_{peak}, simply obtained from a linear interpolation of $\sigma(T) \sim 1/\rho(T)$ (Figs. 4(b)–4(d) in the Appendix and Ref. [8]) between temperatures just above T_{CDW} and well below it [27].

[29] M. Corasaniti, R. Yang, A. Pal, M. Chinotti, L. Degiorgi, A. Wang, and C. Petrovic, Fermi surface gapping in the Dirac material $Ca_{1-x}Na_xMnBi_2$, Phys. Rev. B **100**, 041107(R) (2019).

[30] M. Chinotti, J. Ethiraj, C. Mirri, X. Zhu, L. Li, C. Petrovic, and L. Degiorgi, Impact of the charge density wave state in the electrodynamic response of $ZrTe_{3-x}Se_x$: Optical evidence for a pseudogap phase, Phys. Rev. B **97**, 045117 (2018).

[31] X. Zhu, W. Ning, L. Li, L. Ling, R. Zhang, J. Zhang, K. Wang, Y. Liu, L. Pi, Y. Ma, H. Du, M. Tian, Y. Sun, C. Petrovic, and Y. Zhang, Superconductivity and charge density wave in $ZrTe_{3-x}Se_x$, Sci. Rep. **6**, 26974 (2016).

[32] A. Schwartz, M. Dressel, B. Alavi, A. Blank, S. Dubois, G. Grüner, B. P. Gorshunov, A. A. Volkov, G. V. Kozlov, S. Thieme, L. Degiorgi, and F. Lévy, Fluctuation effects on the electrodynamics of quasi-one-dimensional conductors above the charge-density-wave transition, Phys. Rev. B **52**, 5643 (1995).

[33] A. Perucchi, L. Degiorgi, and R. E. Thorne, Optical investigation of the charge-density-wave phase transitions in $NbSe_3$, Phys. Rev. B **69**, 195114 (2004).

[34] P. A. Lee, T. M. Rice, and P. W. Anderson, Fluctuation Effects at a Peierls Transition, Phys. Rev. Lett. **31**, 462 (1973).

[35] W. Kohn, Excitonic Phases, Phys. Rev. Lett. **19**, 439 (1967).

[36] T. E. Kidd, T. Miller, M. Y. Chou, and T.-C. Chiang, Electron-Hole Coupling and the Charge Density Wave Transition in $TiSe_2$, Phys. Rev. Lett. **88**, 226402 (2002).

[37] G. Li, W. Z. Hu, D. Qian, D. Hsieh, M. Z. Hasan, E. Morosan, R. J. Cava, and N. L. Wang, Semimetal-to-Semimetal Charge Density Wave Transition in $1T$-$TiSe_2$, Phys. Rev. Lett. **99**, 027404 (2007).

[38] R. G. Moore, V. Brouet, R. He, D. H. Lu, N. Ru, J.-H. Chu, I. R. Fisher, and Z.-X. Shen, Fermi surface evolution across multiple charge density wave transitions in $ErTe_3$, Phys. Rev. B **81**, 073102 (2010).

[39] S. Kasahara, H. J. Shi, K. Hashimoto, S. Tonegawa, Y. Mizukami, T. Shibauchi, K. Sugimoto, T. Fukuda, T. Terashima, A. H. Nevidomskyy, and Y. Matsuda, Electronic nematicity above the structural and superconducting transition in $BaFe_2(As_{1-x}P_x)_2$, Nature (London) **486**, 382 (2012).

[40] L. Nie, K. Sun, W. Ma, D. Song, L. Zheng, Z. Liang, P. Wu, F. Yu, J. Li, M. Shan, D. Zhao, S. Li, B. Kang, Z. Wu, Y. Zhou, K. Liu, Z. Xiang, J. Ying, Z. Wang, T. Wu *et al.*, Charge-density-wave-driven electronic nematicity in a Kagome superconductor, Nature (London) **604**, 59 (2022).

[41] L. Zheng, Z. Wu, Y. Yang, L. Nie, M. Shan, K. Sun, D. Song, F. Yu, J. Li, D. Zhao, S. Li, B. Kang, Y. Zhou, K. Liu, Z. Xiang, J. Ying, Z. Wang, T. Wu, and X. Chen, Emergent charge order in pressurized Kagome superconductor CsV_3Sb_5, Nature (London) **611**, 682 (2022).